Transient mobilization of subcrustal carbon coincident with Palaeocene–Eocene Thermal Maximum

Thomas M. Gernon [1 ✉], Ryan Barr[1], J. Godfrey Fitton[2], Thea K. Hincks [1], Derek Keir[1,3], Jack Longman [1,4], Andrew S. Merdith [5,6], Ross N. Mitchell [7] and Martin R. Palmer [1]

Plume magmatism and continental breakup led to the opening of the northeast Atlantic Ocean during the globally warm early Cenozoic. This warmth culminated in a transient (170 thousand year, kyr) hyperthermal event associated with a large, if poorly constrained, emission of carbon called the Palaeocene–Eocene Thermal Maximum (PETM) 56 million years ago (Ma). Methane from hydrothermal vents in the coeval North Atlantic Igneous Province (NAIP) has been proposed as the trigger, though isotopic constraints from deep sea sediments have instead implicated direct volcanic carbon dioxide (CO_2) emissions. Here we calculate that background levels of volcanic outgassing from mid-ocean ridges and large igneous provinces yield only one-fifth of the carbon required to trigger the hyperthermal. However, geochemical analyses of volcanic sequences spanning the rift-to-drift phase of the NAIP indicate a sudden ~220 kyr-long intensification of magmatic activity coincident with the PETM. This was likely driven by thinning and enhanced decompression melting of the sub-continental lithospheric mantle, which critically contained a high proportion of carbon-rich metasomatic carbonates. Melting models and coupled tectonic–geochemical simulations indicate that $>10^4$ gigatons of subcrustal carbon was mobilized into the ocean and atmosphere sufficiently rapidly to explain the scale and pace of the PETM.

During the early Cenozoic, a major episode of continental breakup in the northeast Atlantic (Fig. 1a) resulted in widespread magmatism and the opening of the northeast Atlantic Ocean[1,2]. Initially, continental extension above the Iceland plume caused rifting and an associated phase of subaerial volcanism lasting ~5 million years (Myr) (refs. [3–6]). By ~56 Ma, rifting had progressed to near continental breakup[1] (Fig. 1d), coinciding with an order of magnitude increase in melt production rates[2] and accelerated westward migration of Greenland[7] (Fig. 1e). This transitional phase of volcanism in the North Atlantic Igneous Province (NAIP) involved peak eruption rates of ~2.4 km³ yr⁻¹ (ref. [4]) and occurred contemporaneously with intense early Eocene warming, including the Palaeocene–Eocene Thermal Maximum (PETM)[8]. Expansion of the northeast Atlantic then continued through mid-ocean ridge spreading[1,5] (Fig. 1b,d,e).

During the PETM, sea surface temperatures increased by ~5 °C (ref. [9]), ocean acidification occurred[10,11] and there was a geologically abrupt negative $\delta^{13}C$ carbon isotope excursion that lasted about 170 thousand years (kyr)[8,12] (Fig. 1c). It is thought that the release of approximately $1–1.5 \times 10^4$ gigatons (Gt) of carbon into the ocean–atmosphere system is necessary to account for these changes[11,13]. This massive carbon flux has been attributed to methane release ($\delta^{13}C$ −60‰) associated with clathrate destabilization along continental shelves[14] and hydrothermal venting during interaction of magmas and organic-rich mudrocks ($\delta^{13}C$ −35‰ to −50‰) (ref. [15]). Simulations of the latter process predict peak emissions of 0.2–0.5 Gt C per year, potentially potent enough to drive

PETM warming[16]. Alternatively, based on paired $\delta^{11}B–\delta^{13}C$ data and carbon-cycle modelling[11] and B/Ca in planktic foraminifera[13], it has been proposed that triggering of the PETM required the injection—over about 50 kyr—of an isotopically heavier source of carbon ($\delta^{13}C$ −11‰), most likely tied to volcanic outgassing across the NAIP[11]. Under this scenario, considerably more carbon is required from magmatic and volcanic sources to drive the negative $\delta^{13}C$ excursion than is required from a methane/organic carbon source. Hence, it remains unclear whether NAIP magmatism could contribute enough CO_2 on sufficiently short timescales (10s to 100s kyr) to initiate PETM warming, especially given that this magmatism occurred over several million years[1,2,11,15]. Critically, how carbon emissions were distributed over this interval is unknown[11].

Quantifying background volcanic CO_2 fluxes

We quantitatively estimated the combined CO_2 emissions from incipient mid-ocean ridge volcanism and large igneous provinces (LIPs) in the NAIP, parameterized by plate tectonic reconstructions (Fig. 1b,d) and existing estimates of magmatic productivity[4] (Methods). In our model, we considered pre-eruptive CO_2 concentrations of 2 wt%, which are typical of flood basalt eruptions[17]. The associated CO_2 release from the ocean crust is then calculated from the ratio between the observed levels of magmatic production along the present day mid-ocean ridge system (~18 km³ per year) and estimated CO_2 degassing fluxes along the modern global ridge system (7×10^{11} mol per year) (ref. [18]). This calculation suggests that ~10% of the CO_2 in the juvenile ocean crust is degassed

[1]School of Ocean & Earth Science, University of Southampton, Southampton, UK. [2]School of GeoSciences, University of Edinburgh, Edinburgh, UK. [3]Dipartimento di Scienze della Terra, Università degli Studi di Firenze, Florence, Italy. [4]Institute for Chemistry & Biology of the Marine Environment, University of Oldenburg, Oldenburg, Germany. [5]Laboratoire de Géologie, Université de Lyon 1, Villeurbanne, France. [6]School of Earth and Environment, University of Leeds, Leeds, UK. [7]State Key Laboratory of Lithospheric Evolution, Institute of Geology & Geophysics, Chinese Academy of Sciences, Beijing, China. ✉e-mail: Thomas.Gernon@noc.soton.ac.uk
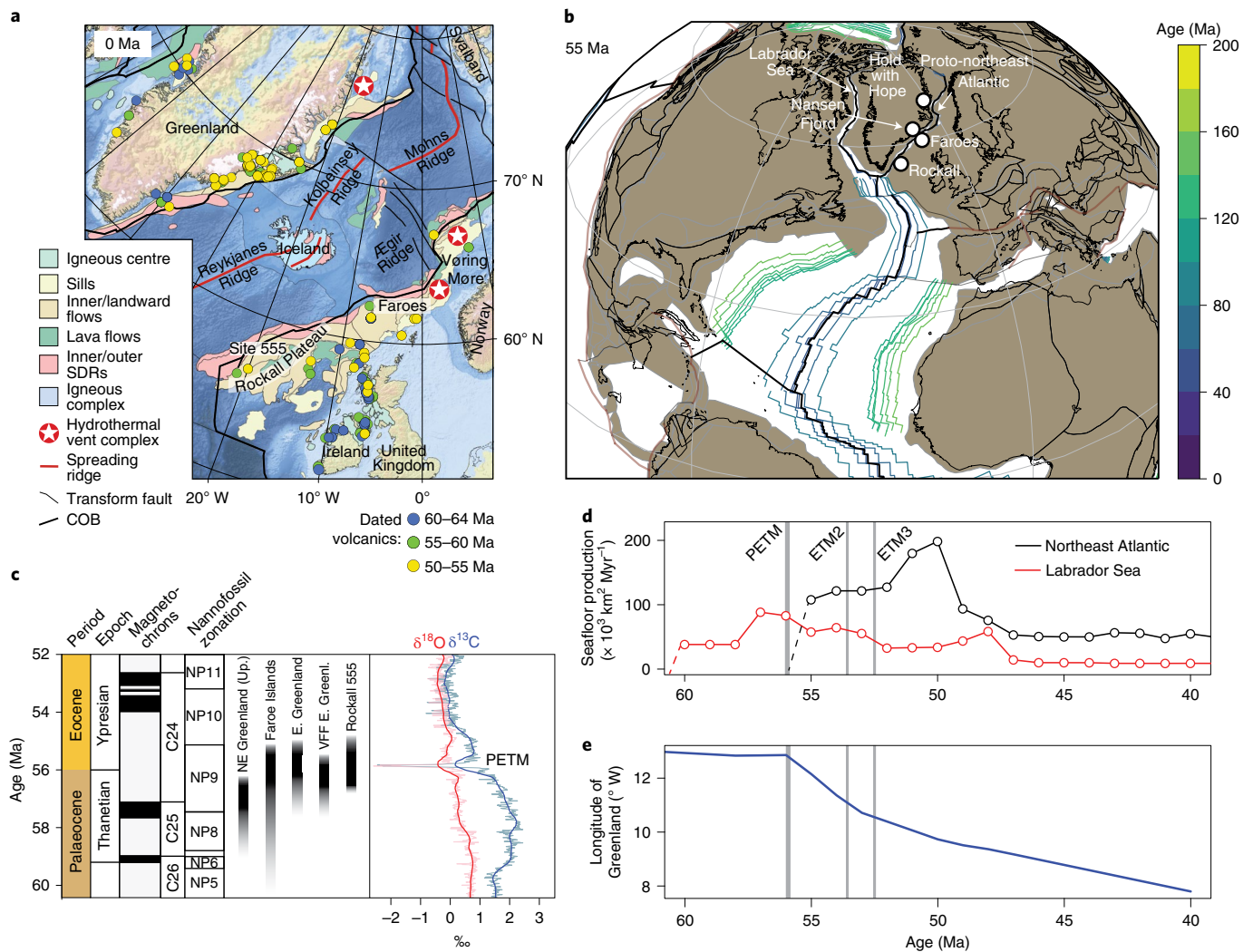
Fig. 1 | Early Cenozoic tectonic and magmatic evolution of the northeast Atlantic. a, Map of the present day northeast Atlantic region showing the distribution of Palaeocene–Eocene lava flows and intrusives, with dated volcanics denoted by coloured symbols and the locations of major hydrothermal vent complexes in the Vøring and Møre Basins[15] and offshore Northeast Greenland[54] shown as stars (SDRs = seaward-dipping reflectors; COB = continent–ocean boundary). **b**, Plate tectonic reconstruction showing nascent ridge systems developing along the Labrador Sea and northeast Atlantic at 55 Ma; the perimeter to brown shaded regions shows continent-ocean boundaries, and brown lines signify subduction zones (Methods). **c**, Ages of the volcanic sections discussed (Up. = Upper; VFF = Vandfaldsdalen Fm, E. = East, Greenl. = Greenland), defined by radiometric dates[1,2], magnetostratigraphy and nannofossil zonation[22,25,37] and corresponding carbon and oxygen isotope records showing the PETM isotope excursions (solid and faint lines show 1 Myr and 20 kyr locally weighted functions, respectively)[55]. **d**, Seafloor production rates for the Labrador Sea and northeast Atlantic, derived from GPlates (Methods), shown alongside the timing of Eocene hyperthermals (PETM and Eocene Thermal Maximum (ETM) 2 and 3). **e**, Palaeolongitude of Greenland[7], indicating the onset of ocean crustal production in the Northeast Atlantic at 56 Ma. Panel **a** is adapted with permission from ref. [3], Springer Nature Limited.

at ridges. Using this estimate, the NAIP ridges probably produced ~1.1×10^3 Gt C during the PETM. This is an order of magnitude lower than the requisite ~1–1.5×10^4 Gt C (refs. [11,13]). Inclusion of the effects of LIP magmatism—assuming most probable eruption rates[4] and total degassing—yields less than one-fifth of the carbon needed to drive and sustain the PETM[11,13]. Furthermore, seafloor isochrons indicate that magmatic productivity along the northeast Atlantic ridge peaked after, not during, early Eocene hyperthermals (Fig. 1d). Therefore, some other major, but transient, source of volcanic carbon appears to be required if the volcanic outgassing hypothesis[11,13] is correct.

Spatial and temporal characteristics of PETM volcanism
We investigated several volcanic sequences spanning the Palaeocene–Eocene boundary (Fig. 1c). The Deep Sea Drilling Project Leg 81 Site 555 lies on the Rockall Plateau (Fig. 1a), with

volcanics extruded just before breakup in the proto-northeast Atlantic (Fig. 1b). Here 'Phase 1' volcanism[19] (Fig. 2a and Extended Data Figs. 1 and 2) is coeval with the Milne Land basalts in East Greenland and the Middle- to Upper-Series lavas in the Faroe Islands[1] (Fig. 2b–c). In the Rockall sequence, we found a sharp increase in the frequency of volcanic tuffs just below the Palaeocene–Eocene boundary (Fig. 2a) (Methods). The PETM is defined by $\delta^{13}C$, however the volcanostratigraphy in our study area is not conducive to developing a high-resolution carbon isotope stratigraphy (Methods). Therefore, we rely on a combination of radiometric, magnetostratigraphic and palaeontological age constraints, in addition to existing sediment accumulation rate estimates (Methods). Mudstones interbedded with the uppermost tuffs are thought to contain the dinoflagellate cyst, *Apectodinium augustum*[20], which signifies a sudden prevalence of tropical sea surface temperatures linked to PETM warming[21]. On the basis of sedimentation rates
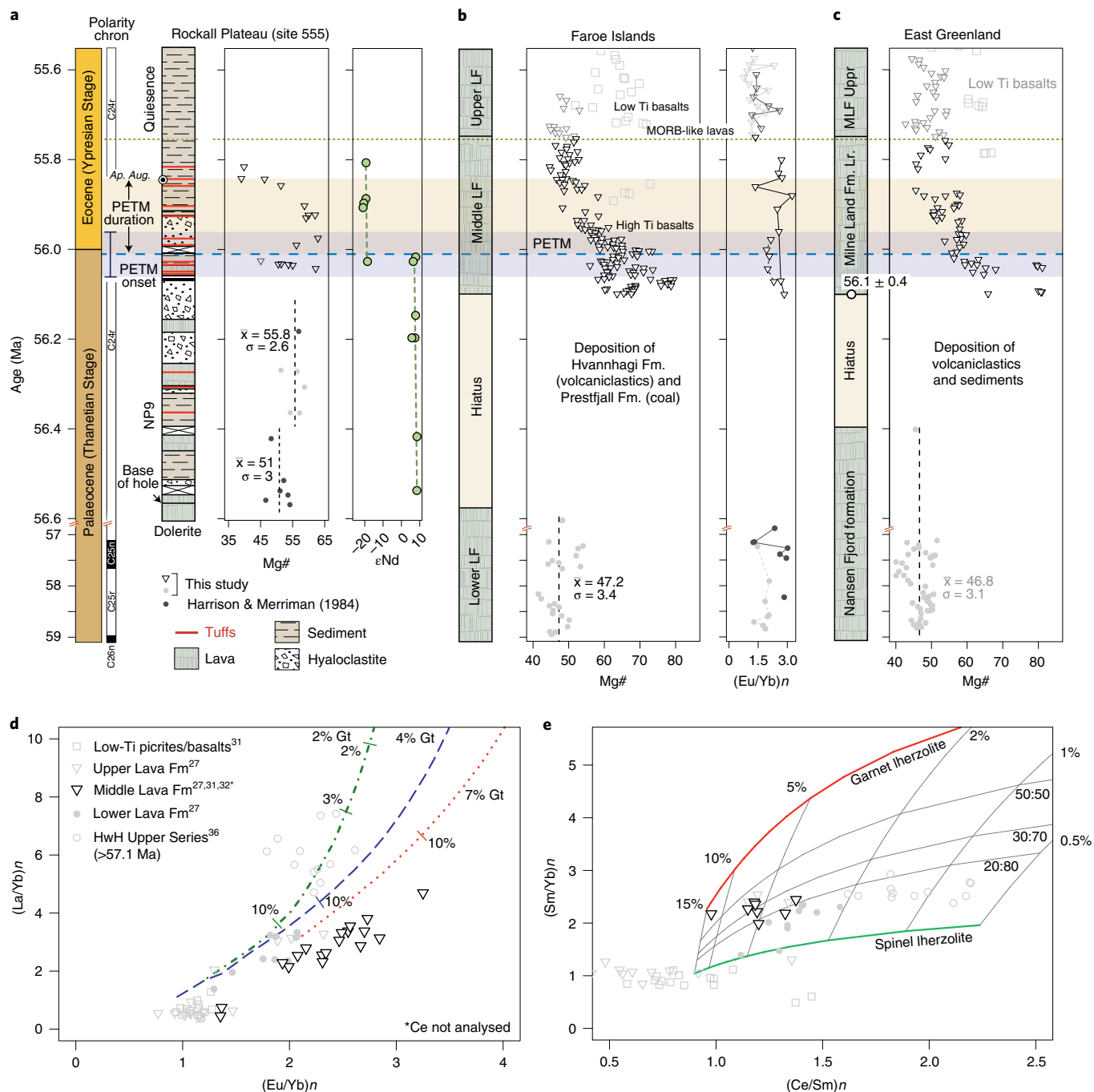
Fig. 2 | Palaeocene–Eocene volcanostratigraphy and geochemistry of the proto-northeast Atlantic ridge. a, Simplified log of the Rockall 'Phase 1' sequence[19] showing lithologies, Mg# (that is, $100 \times$ molecular $MgO/(MgO + FeO)$, where FeO is assumed to be $0.9FeOT$) and ϵNd (Extended Data Fig. 1). Please note the scale break at 56.6 Ma; the vertical dashed lines in panels (**a**) to (**c**) show mean ($\bar{x}$) values for variables over the intervals shown. **b,c**, Simplified log of the Faroes Basalt formations[26] (**b**), with Mg# and (Eu/Yb)n (chondrite-normalized[56]); Mg# data are from ref. [26] and (Eu/Yb)n are from refs. [27,32] (Extended Data Fig. 2); note the sharp transition to high Mg# (and enriched rare earth element contents) at ca. 56.1 Ma[1], which is also observed in east Greenland (Milne Land Formation)[26] MORB, mid-ocean ridge basalt; Fm., formation. (**c**). **d**, (La/Yb)n versus (Eu/Yb)n of the Faroes and Hold with Hope (HwH) lavas (chondrite-normalized[56]) and modelled non-modal batch melting of a lherzolitic mantle source, adopted from ref. [33], showing different degrees of melting of a garnet lherzolite (green, blue and red curves). **e**, (Sm/Yb)n versus (Ce/Sm)n and a rare earth element melting model (Methods), showing percentage melt along the top and the relative proportions of garnet- and spinel-lherzolites from 100% gt-lherzolite (red curve) to 100% sp-lherzolite (green curve). Both models indicate that the Faroes Middle Lava Formation (that is, high-Mg# basalts in the lower 500 m of the Middle Lavas; see **b**), which erupted immediately before and during the PETM, experienced the highest degrees of melting of a mantle source containing ≳10% garnet.

$(50 \, cm \, ka^{-1})$ (ref. [22]), this volcanic flare-up lasted for 171–213 kyr, similar to the duration of the coeval PETM[8,12] and was followed by a sharp decline in volcanism[19]. The tuffs exhibit wide compositional

diversity from basanites to dacites (Extended Data Figs. 1, 3a–b and Extended Data Tables 1–3), an increased range of magnesium number (Mg#; ≲63), and a marked shift to highly negative ϵNd

signatures at ca. 56.03 Ma (Fig. 2a). This activity signals a step change in magmatic processes and volcanic unrest along the rift, as recorded across a major area of the NAIP (>130,000 km²) (refs. [1,23]). Sampled PETM-age tuffs are enriched in Rb and Ba and depleted in Nb and Sr (Extended Data Fig. 3c and Extended Data Table 3), and most have similar compositions to some of the lowermost ('negative ash series') tuffs of the Danish Basin, thought to derive from nearby volcanoes along the continental shelf[23]. However, the very negative ϵNd values of some of the uppermost tuffs (Fig. 2a and Extended Data Table 2) probably reflect assimilation of ancient continental crust and suggest that they were derived from a Greenland source[24]. Taken together, this is consistent with the observed intensification of volcanic activity across the wider NAIP during the PETM[25] (Fig. 1a).

Interpretation of geochemical data from the Rockall tuffs is complicated because they derive from a range of sources and have experienced varying degrees of seafloor weathering[19]. Hence, we next studied the coeval thick basaltic lava sequences that were emplaced subaerially near the rift axis (Fig. 1). The Palaeocene–Eocene lavas of the Faroe Islands and East Greenland (Fig. 1b) are ideally suited because, unlike the contemporaneous lavas in SE Greenland[24], they are minimally affected by crustal contamination[26–29]. The base of the Milne Land Formation in East Greenland, which correlates with the base of the Middle Lava Series (also known as the Malinstindur Formation[30]) of the Faroes[1,26] (Fig. 2b,c; hereafter both referred to as the 'Middle Lavas'), is dated at 56.1 ± 0.4 Ma, and the duration of activity is reasonably well constrained[1,2] (Fig. 2). Thus, the base of the Middle Lavas correlates with (or shortly predates) the intensification of volcanism at Rockall Plateau (Fig. 2a).

We estimate that the 1.25 km-thick Middle Lavas[1,26] were emplaced over 200–300 kyr (Fig. 2b–c; Methods), yielding an average eruption rate of ~4–6 m kyr⁻¹ but potentially an order of magnitude higher early in the eruptive cycle[1]. At the base of the sequence, thick (>100 m) pyroclastic deposits, also reported in Greenland[26], signal an early volatile-rich explosive phase[29]. The overlying tholeiitic lavas are characterized by a sharp increase in Mg#, from values of ~52 throughout the Lower Lava Formation[26] to >80 in the basal part of the Middle Lavas (Fig. 2b,c). The basal lavas are coincident (within dating uncertainties) with the onset of the PETM[8]. Many of these lavas are highly magnesian[31] (for example, with MgO = 24%), implying hot liquidus temperatures and are locally characterized by massive olivine accumulation[26,29]. They also exhibit high TiO_2 contents (typically 1.5–2.5 wt.%), and enrichment in light rare earth elements, for example, (La/Yb)$_n$ = 2–3 and (Eu/Yb)$_n$ > 2.5 (Fig. 2b)[27,32]. This unusual pulse of high-Ti magmatism, similar to that of the Jurassic Karoo flood basalts in southern Africa[33], generated the long-lived (~300 kyr) (ref. [1]) Skaergaard layered igneous intrusion at 55.75 ± 0.35 Ma (Fig. 1a)[1]. Finally, the Upper Lava Formation (Fig. 2b,c) signifies an abrupt shift to low-Ti depleted MORB-like lavas[26,27,32] (Fig. 2d,e). Their age and diagnosis as mid-ocean ridge basalts (MORB) are consistent with independent geotectonic constraints for onset of seafloor production between 56–55 Ma (Fig. 1d,e). Thus, there is evidence that the early volcanism responsible for the PETM-aged high-Mg# Middle Lavas was both transient[1] (~227 kyr) and chemically anomalous (Fig. 2).

The geochemical compositions of these lavas have been attributed to partial melting of the subcontinental lithospheric mantle (SCLM) during asthenospheric upwelling[27], a model that is supported by studies of their feeder intrusions[28,31]. To test this hypothesis further, we applied two models of mantle melting. First, we adopted a non-modal batch melting model of a garnet-bearing lherzolitic mantle source[33] (Fig. 2d). For the second model, we estimated melt percentage based on average lherzolite mineralogy, average partition coefficients and a plume composition based on primitive basalt (Fig. 2e) (Methods and Extended Data Table 4). Both models suggest that the Middle Lavas derived from a high degree of melting,
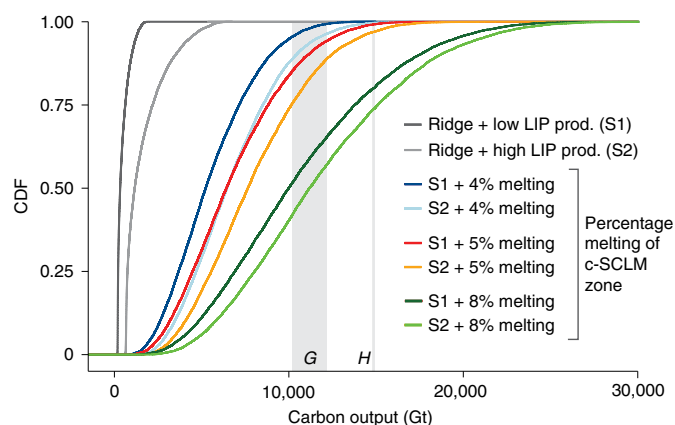

Fig. 3 | Simulations of volcanic carbon release during the PETM. Results are plotted as cumulative distribution functions (CDFs). The grey lines show the estimated carbon output from ridge volcanism and LIPs alone; with S1 and S2 showing low (0.6 km³ per year) and high (2.4 km³ per year) LIP volcanic productivity (prod.) scenarios[4], respectively (Extended Data Fig. 4 and Methods). The coloured lines show the effects of adding 4% to 8% carbonated (c-) SCLM melt along the incipient ridge during breakup. The grey vertical bars denote the carbon output necessary to drive and sustain PETM warming estimated by Gutjahr et al.[11] (labelled G; 10,200–12,200 Gt C) and Haynes and Hönisch[13] (labelled H; 14,900 Gt C).

up to ~13% but typically in the range of 4–8%, with their high (Sm/Yb)$_n$ ratios (2–2.5) requiring ~20% to >50% of garnet lherzolite in the mantle source (Fig. 2e). Metasomatism in the mantle source has already been documented in this region[34] and invoked to explain the compositional characteristics of these high-Ti basalts, notably their light rare earth element enrichment and variable Nb and Ta anomalies[28,31]. The compositions of the Middle Lavas are compatible with enhanced melting of metasomatized SCLM by the Iceland plume[32], immediately before and during continental breakup and therefore just before seafloor spreading at ca. 55.8 Ma (Fig. 2b,c). This short-lived phase of elevated melting—as observed in other rifts globally (for example, ref. [35])—is supported by the peak in crustal P wave velocity (7.5 km s⁻¹) across the continental–ocean transition of the northeast Atlantic margins[6]. This peak straddles the seaward side of the continental–ocean transition and likely results from intrusion of similarly high-Mg mafic melts related to increased melting just before continental breakup[6].

Trace element compositions show that the degree of melting varies systematically through the Faroes sequence (Fig. 2e), with the Lower Lava Formation (Fig. 2b,c) representing a relatively low degree of melting (2–5%; Fig. 2e). To expand the dataset, lavas from farther along the rift axis in northeast Greenland are included (Hold with Hope)[36] (Fig. 1b), which have an upper age of ca. 57 Ma (C25n–C24r)[5]. These lavas exhibit geochemical characteristics that have been attributed to the incorporation of SCLM during melting[5,36]. Our model confirms a low degree of melting (0.5–2%) of a variably garnet-rich lherzolite source (Fig. 2e). Taken together, these observations confirm an up-section increase in the involvement of SCLM in melting during the late Palaeocene, peaking just before the PETM (Fig. 2e), then rapidly declining in intensity before the onset of seafloor spreading. There is possible evidence for this peak in Palaeocene–Eocene[37] basaltic lavas of the Vandfaldsdalen Formation in central east Greenland[38]. These lavas exhibit Nd, Sr and Pb isotope signatures indicative of an SCLM component, with limited crustal contamination[38]. Assimilation of the deep SCLM is particularly important because this zone is metasomatically enriched in carbonates and is thus a major carbon reservoir[39–42].
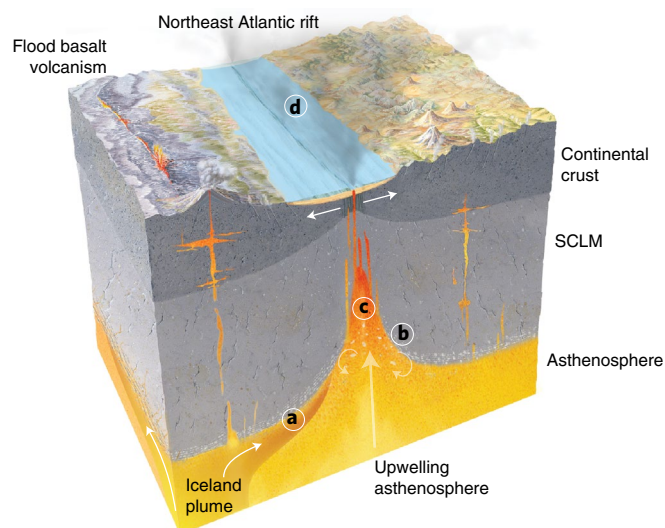
Fig. 4 | Deep carbon mobilization and release in the North Atlantic during the PETM. The model stages are shown. **a**, Thermomechanical weakening of the SCLM by the Iceland plume. **b**, Thermal removal, delamination and lateral advection of metasomatized SCLM (shown as the white stippled pattern) by edge-driven convection in the asthenospheric mantle. **c**, Carbonate-rich domains are entrained into the central melt zone beneath the evolving rift, where they are thermodynamically unstable and involved in transient decompression melting just before continental breakup. **d**, Massive outgassing of CO_2 at Earth's surface from the northeast Atlantic rift and associated volcanic and tectono–magmatic systems. Credit: Gary Hincks.

Mobilization of lithospheric mantle carbon

Rifting severely disrupts the >100 km-thick cratonic lithosphere[43]. Because carbonates are only stable in the mantle at high pressures (~3 GPa at a temperature of 1,300 °C) (ref. [43]), substantial carbon release will occur only when extending cratons are 130 km thick or more[43]. Seismic tomography indicates that the lithosphere in central Greenland (that is, the locus of the Iceland plume at 56 Ma (ref. [3])) is 180 km thick[44], firmly meeting this criterion. Peridotite xenoliths provide evidence for metasomatism in the deep SCLM beneath Greenland[34], as does the occurrence of strongly alkaline and carbonatitic magmatism across the wider NAIP in the early Cenozoic[45]. Therefore, breakup of the North Atlantic craton provided a combination of conditions optimal for carbon release: continental rifting of sufficiently thick cratonic lithosphere thermo-mechanically weakened by the Iceland mantle plume[3] (Figs. 3 and 4a and Extended Data Fig. 4) allowed for the melting of deep, carbonate-rich domains of SCLM[40,41,43]. This is in some ways analogous to the carbon-release scenario proposed for the Siberian Traps, linked to the Permo–Triassic extinction event[42]. Thickening of such carbonate-enriched SCLM is thought to occur during supercontinent formation, followed by thermal re-equilibration resulting in warming and conversion to asthenosphere[46]. During continental breakup, this enriched and heated asthenosphere is then channelled into thinner parts of the continental and oceanic lithosphere, where it experiences decompression melting[46].

Both the thickness and composition of the early Cenozoic NAIP lithospheric mantle make it a viable source of large amounts of carbon from the deep, carbonated SCLM. A key aspect of our hypothesis is that the most extensive period of CO_2 outgassing (~50 Mt C per year) occurred over a short period (~200 kyr) and most likely peaked just before PETM onset (Fig. 2b,c). In our model, continental rifting of thick lithosphere generates a steep lithosphere–asthenosphere boundary (Fig. 4). This promotes edge-driven convection in the asthenospheric mantle[40,47,48] that gives rise to lateral advection

of metasomatized SCLM[39,47] into a zone of intense decompression melting that extends deep (~150 km) (Fig. 4b). Numerical models predict this transient phase of deep decompression melting to occur during the final stages of breakup, 6–7 Myr after rifting onset[43], which is remarkably consistent with the inferred increase in deep melting just before breakup[6] (Figs. 2d,e) and its timing relative to NAIP onset[5]. Because alteration zones permeate the lowermost SCLM, it is weak and prone to thermal erosion and delamination at the step change in cratonic lithosphere thickness[40] (Fig. 4). This facilitates detachment of metasomatic domains and entrainment into the melt zone beneath the evolving rift (Fig. 4c) where pressures are lower, temperatures are higher and metasomatic carbonates are thermodynamically unstable, releasing CO_2[39,43]. Indeed, it has been suggested that relics of such metasomatic material that delaminated during northeast Atlantic rifting can explain residual enriched 'EM1' components still present in the Icelandic mantle today[49–51]. The question is then whether this process can contribute enough carbon to help explain the PETM carbon isotope excursion.

Recent estimates suggest that the SCLM may contain 5–8% CO_2 or possibly more[41]. To quantify the potential influence of rift-related SCLM disturbance, we performed 10,000 Monte Carlo calculations using CO_2 contents ranging from 1–8% and length scales of the carbonated SCLM in the narrow melting zone below the rift near breakup[43] based on tectonic reconstructions, chemical tomography and lithospheric models (Methods and Extended Data Tables 5 and 6). These calculations suggest that only 4–8% of this zone needs to melt to exceed the requisite $>10^4$ Gt C for PETM warming[11,13] (Fig. 3). This is consistent with the modelled 5–8% melting of a garnet-rich lherzolite during the PETM (Fig. 2d,e) and earlier estimates that the intrusive feeders of these Ti-rich basalts formed by 4% (ref. [31]) to 7% (ref. [28]) batch melting of fertile, metasomatized lherzolites in the SCLM[28]. In summary, our data suggest that rift evolution enabled the distinct peak in melt supply and volcanism just before breakup (evident in the compositional characteristics of thick lava piles; Fig. 2), with vigorous decompression melting of entrained SCLM and subsequent upward migration of CO_2 (Fig. 4). This CO_2 was delivered to the atmosphere via degassing from active volcanic sources (including subaerial flood basalts and along the rift axis), crustal magmatism and deep extensional fault systems that define active rifts[52] (Fig. 4d).

Northeast Atlantic volcanism and climate change

The step change in NAIP magmatic productivity[2] immediately before the PETM gave rise to widespread magmatic and volcanic unrest (Figs. 2 and 4). Whereas some volcanic tuffs at Rockall Plateau are probably linked to the Middle Lavas (especially those with high Mg#), many of these tuffs are probably genetically unrelated but are rather a manifestation of the general increase in mantle melting and fluxes of magma and volatiles through magmatic systems along the continental shelf and Greenland continental margin at this time[23]. The Rockall sequence places firm constraints on both the timing and duration of this climate-altering phase of volcanism at ~171–213 kyr, which is similar to the duration of the lower, high Mg#, part of the Middle Lavas (Fig. 2). This surge in regional volcanic activity could explain the wide variability in the composition of tuffs belonging to the Danish negative ash series[23]. Indeed, the chemical weathering of extensive tephra blankets may also explain the large decrease in $^{187}Os/^{188}Os$ ratios observed in sediments just before PETM onset at Svalbard[53].

Enhanced melting of the SCLM during continental breakup resulted from an unusual combination of conditions in the NAIP (Fig. 4) and provides a direct mechanism to dramatically increase the outgassing of deep carbon. Our data suggest that enhanced mantle melting and the release of deep carbon most likely reached peak intensity just before PETM onset (Fig. 2), which is consistent with other independent evidence for a massive surge of $\delta^{13}C$-depleted

carbon[11,13] (Fig. 3). Melting of deep, carbonate-rich domains of the SCLM can result in a fivefold increase in magmatic CO_2 output, providing a powerful mechanism to boost short-term CO_2 degassing and reconciling an apparent major deficit of carbon from 'background' ridge and LIP magmatism (Fig. 3). This enhanced mantle melting occurred contemporaneously with methane release from hydrothermal vents related to the same phases of magmatism[15,16,54], which potentially supplied an isotopically lighter end member to the PETM carbon cycle[11]. Our study supports the proposal that large-scale lithospheric melting can induce global warming[42] if the tectonic setting is primed to facilitate intensive magmatic CO_2 release (Fig. 4). This highlights the critical role that solid Earth degassing plays in driving abrupt hyperthermal events such as the PETM, promoting fundamental reorganization of Earth's surface environment and biosphere.

Online content

Any methods, additional references, Nature Research reporting summaries, source data, extended data, supplementary information, acknowledgements, peer review information; details of author contributions and competing interests; and statements of data and code availability are available at https://doi.org/10.1038/s41561-022-00967-6.

References

1. Storey, M., Duncan, R. A. & Swisher, C. C. Paleocene–Eocene Thermal Maximum and the opening of the northeast Atlantic. *Science* **316**, 587–589 (2007).
2. Storey, M., Duncan, R. A. & Tegner, C. Timing and duration of volcanism in the North Atlantic Igneous Province: implications for geodynamics and links to the Iceland hotspot. *Chem. Geol.* **241**, 264–281 (2007).
3. Steinberger, B., Bredow, E., Lebedev, S., Schaeffer, A. & Trond, H. T. Widespread volcanism in the Greenland–North Atlantic region explained by the Iceland plume. *Nat. Geosci.* **12**, 61–68 (2019).
4. Eldholm, O. & Grue, K. North Atlantic volcanic margins: dimensions and production rates. *J. Geophys. Res.* **99**, 2955–2968 (1994).
5. Saunders, A. D., Fitton, J. G., Kerr, A. C., Norry M. J. & Kent, R. W. in *Large Igneous Provinces* Vol. 100 (eds Mahoney, J. J. & Coffin, M. F.) 45–94 (AGU, 1997).
6. White, R. S. et al. Lower-crustal intrusion on the North Atlantic continental margin. *Nature* **452**, 460–464 (2008).
7. Mitchell, R. N., Kilian, T. M. & Evans, D. A. D. Supercontinent cycles and the calculation of absolute palaeolongitude in deep time. *Nature* **482**, 208–211 (2012).
8. Zeebe, R. E. & Lourens, L. J. Solar system chaos and the Paleocene–Eocene boundary age constrained by geology and astronomy. *Science* **365**, 926–929 (2019).
9. Frieling, J. et al. Extreme warmth and heat-stressed plankton in the tropics during the Paleocene–Eocene Thermal Maximum. *Sci. Adv.* **3**, e1600891 (2017).
10. Zachos, J. C., Dickens, G. R. & Zeebe, R. E. An early Cenozoic perspective on greenhouse warming and carbon-cycle dynamics. *Nature* **451**, 279–283 (2008).
11. Gutjahr, M. et al. Very large release of mostly volcanic carbon during the Palaeocene–Eocene Thermal Maximum. *Nature* **548**, 573–577 (2017).
12. Röhl, U., Westerhold, T., Bralower, T. J. & Zachos, J. C. On the duration of the Paleocene–Eocene Thermal Maximum (PETM). *Geochem. Geophys. Geosyst.* **8**, Q12002 (2007).
13. Haynes, L. L. & Hönisch, B. The seawater carbon inventory at the Paleocene–Eocene Thermal Maximum. *Proc. Natl Acad. Sci. USA* **117**, 24088–24095 (2020).
14. Dickens, G. R., O'Neil, J. R., Rea, D. K. & Owen, R. M. Dissociation of oceanic methane hydrate as a cause of the carbon isotope excursion at the end of the Paleocene. *Paleoceanography* **10**, 965–971 (1995).
15. Svensen, H. et al. Release of methane from a volcanic basin as a mechanism for initial Eocene global warming. *Nature* **429**, 542–545 (2004).
16. Jones, S. M., Hoggett, M., Greene, S. E. & Dunkley Jones, T. Large igneous province thermogenic greenhouse gas flux could have initiated Paleocene–Eocene Thermal Maximum climate change. *Nat. Commun.* **10**, 5547 (2019).
17. Self, S., Thordarson, T. & Widdowson, M. Gas fluxes from flood basalt eruptions. *Elements* **1**, 283–287 (2005).
18. Chavrit, D., Humler, E. & Grasset, O. Mapping modern CO_2 fluxes and mantle carbon content all along the mid-ocean ridge system. *Earth Planet. Sci. Lett.* **387**, 229–239 (2014).
19. Morton, A. C. & Keene, J. B. in *Initial Reports DSDP* Vol. 81 (eds Roberts, D. G. et al.) Ch. 19 (US Government Printing Office, 1984).
20. Brown, S. & Downie, C. in Initial Reports DSDP Vol. 81 (eds Roberts, D. G. et al.) Ch. 13 (US Government Printing Office, 1984).
21. Sluijs, A. et al. Subtropical Arctic Ocean temperature during the Palaeocene/Eocene thermal maximum. *Nature* **441**, 610–613 (2006).
22. Backman, J. et al. in Initial Reports DSDP Vol. 81 (eds Roberts, D.G. et al.) Ch. 38 (US Government Printing Office, 1984).
23. Larsen, L. M., Fitton, J. G. & Pedersen, A. K. Paleogene volcanic ash layers in the Danish Basin: compositions and source areas in the North Atlantic Igneous Province. *Lithos* **71**, 47–80 (2003).
24. Fitton, J. G., Larsen, L. M., Saunders, A. D., Hardarson, B. S. & Kempton, P. D. Palaeogene continental to oceanic magmatism on the SE Greenland continental margin at 63°N: a review of the results of Ocean Drilling Program Legs 152 and 163. *J. Petrol.* **41**, 951–966 (2000).
25. Stokke, E. W., Jones, M. T., Tierney, J. E., Svensen, H. H. & Whiteside, J. H. Temperature changes across the Paleocene–Eocene Thermal Maximum—a new high-resolution TEX_{86} temperature record from the Eastern North Sea Basin. *Earth Planet. Sci. Lett.* **544**, 116388 (2020).
26. Larsen, L. M., Waagstein, R., Pedersen, A. K. & Storey, M. Trans-Atlantic correlation of the Palaeogene volcanic successions in the Faeroe Islands and East Greenland. *J. Geol. Soc. London* **156**, 1081–1095 (1999).
27. Gariépy, C., Ludden, J. & Brooks, C. Isotopic and trace element constraints on the genesis of the Faeroe lava pile. *Earth Planet. Sci. Lett.* **63**, 257–272 (1983).
28. Hansen, J., Davidson, J., Jerram, D., Ottley, C. & Widdowson, M. Contrasting TiO_2 compositions in early Cenozoic mafic sills of the Faroe Islands: an example of basalt formation from distinct melting regimes. *Earth Sci.* **8**, 235–267 (2019).
29. Millett, J. M., Hole, M. J., Jolley, D. W., Passey, S. R. & Rossetti, L. Transient mantle cooling linked to regional volcanic shut-down and early rifting in the North Atlantic Igneous Province. *Bull. Volcanol.* **82**, 61 (2020).
30. Jolley, D. W., Millett, J. M., Schofield, N., Broadley, L. & Hole, M. J. Stratigraphy of volcanic rock successions of the North Atlantic rifted margin: the offshore record of the Faroe–Shetland and Rockall basins. *Earth Environ. Sci. Trans. R. Soc. Edinburgh* **112**, 61–88 (2021).
31. Holm, P. M., Hald, N. & Waagstein, R. Geochemical and Pb–Sr–Nd isotopic evidence for separate hot depleted and Iceland plume mantle sources for the Paleogene basalts of the Faroe Islands. *Chem. Geol.* **178**, 95–125 (2001).
32. Schilling, J.-G. & Noe-Nygaard, A. Faeroe–Iceland plume: rare-earth evidence. *Earth Planet. Sci. Lett.* **24**, 1–14 (1974).
33. Jourdan, F. et al. Major and trace element and Sr, Nd, Hf, and Pb isotope compositions of the Karoo Large Igneous Province, Botswana–Zimbabwe: lithosphere vs mantle plume contribution. *J. Petrol.* **48**, 1043–1077 (2007).
34. Aulbach, S., Sun, J., Tappe, S., E Höfer, H. & Gerdes, A. Volatile-rich metasomatism in the cratonic mantle beneath SW Greenland: link to kimberlites and mid-lithospheric discontinuities. *J. Petrol.* **58**, 2311–2338 (2018).
35. Bastow, I. D. & Keir, D. The protracted development of the continent–ocean transition in Afar. *Nat. Geosci.* **4**, 248–250 (2011).
36. Thirlwall, M. F., Upton, B. G. J. & Jenkins, C. Interaction between continental lithosphere and the Iceland Plume—Sr–Nd–Pb isotope geochemistry of tertiary basalts, NE Greenland. *J. Petrol.* **35**, 839–879 (1994).
37. Nøhr-Hansen, H. Palynostratigraphy of the Cretaceous–lower Palaeogene sedimentary succession in the Kangerlussuaq Basin, southern East Greenland. *Rev. Palaeobot. Palynol.* **178**, 59–90 (2012).
38. Holm, P. M. Nd, Sr and Pb isotope geochemistry of the Lower Lavas, E Greenland Tertiary Igneous Province. *Geol. Soc. Spec. Publ.* **39**, 181 (1988).
39. Muirhead, J. D. et al. Displaced cratonic mantle concentrates deep carbon during continental rifting. *Nature* **582**, 67–72 (2020).
40. Foley, S. F. Rejuvenation and erosion of the cratonic lithosphere. *Nat. Geosci.* **1**, 503–510 (2008).
41. Foley, S. F. & Fischer, T. P. An essential role for continental rifts and lithosphere in the deep carbon cycle. *Nat. Geosci.* **10**, 897–902 (2017).
42. Sobolev, S. V. et al. Linking mantle plumes, large igneous provinces and environmental catastrophes. *Nature* **477**, 312–316 (2011).
43. Gorczyk, W. & Gonzalez, C. M. CO_2 degassing and melting of metasomatized mantle lithosphere during rifting—numerical study. *Geosci. Front.* **10**, 1409–1420 (2019).
44. Darbyshire, F. A. et al. A first detailed look at the Greenland lithosphere and upper mantle, using Rayleigh wave tomography. *Geophys. J. Int.* **158**, 267–286 (2004).
45. Nielsen, T. F. D. Tertiary alkaline magmatism in East Greenland: a review. *Geol. Soc. Spec. Publ.* **30**, 489 (1987).

46. Guimarães, A. R., Fitton, J. G., Kirstein, L. A. & Barfod, D. N. Contemporaneous intraplate magmatism on conjugate South Atlantic margins: a hotspot conundrum. *Earth Planet. Sci. Lett.* **536**, 116147 (2020).

47. Currie, C. A. & van Wijk, J. How craton margins are preserved: insights from geodynamic models. *J. Geodyn.* **100**, 144–158 (2016).

48. King, S. D. & Anderson, D. L. Edge-driven convection. *Earth Planet. Sci. Lett.* **160**, 289–296 (1998).

49. Debaille, V. et al. Primitive off-rift basalts from Iceland and Jan Mayen: Os-isotopic evidence for a mantle source containing enriched subcontinental lithosphere. *Geochim. Cosmochim. Acta* **73**, 3423–3449 (2009).

50. Torsvik, T. H. et al. Continental crust beneath southeast Iceland. *Proc. Natl Acad. Sci. USA* **112**, E1818 (2015).

51. Hanan, B. B. & Schilling, J. G. The dynamic evolution of the Iceland mantle plume: the lead isotope perspective. *Earth Planet. Sci. Lett.* **151**, 43–60 (1997).

52. Lee, H. et al. Massive and prolonged deep carbon emissions associated with continental rifting. *Nat. Geosci.* **9**, 145–149 (2016).

53. Wieczorek, R., Fantle, M. S., Kump, L. R. & Ravizza, G. Geochemical evidence for volcanic activity prior to and enhanced terrestrial weathering during the Paleocene Eocene Thermal Maximum. *Geochim. Cosmochim. Acta* **119**, 391–410 (2013).

54. Reynolds, P. et al. Hydrothermal vent complexes offshore Northeast Greenland: a potential role in driving the PETM. *Earth Planet. Sci. Lett.* **467**, 72–78 (2017).

55. Westerhold, T. et al. An astronomically dated record of Earth's climate and its predictability over the last 66 million years. *Science* **369**, 1383–1387 (2020).

56. Boynton, W. V. and Henderson, P. in *Cosmochemistry of the Rare Earth Elements: Meteorite Studies* Vol. 2. Ch. 3 (Elsevier, 1984).

Methods

Calculating seafloor production rates. Seafloor production (SP) rates (Fig. 1d), which were utilized in our volcanic CO_2 flux calculations, were calculated using the plate model of Müller et al. (2016)[57] shown in Fig. 1b. We used the open source Python library, 'pyGPlates' (https://www.gplates.org/docs/pygplates/) to filter and extract the data from the plate model. For the target time steps (t, in Myr), we broke the complete mid-ocean ridge system into a series of spreading and transform segments to isolate the spreading segments (j) where new oceanic crust is formed. This approach has recently become common in analysing tectonic scenarios in ocean basins[58–61]. At each segment for each time step, we extracted the full spreading rate (u, in km Myr^{-1}) and the length of the spreading segment (L, in km). The full spreading rate was calculated by summing the half spreading rate of each individual flank of each ridge segment, thereby sidestepping any issues pertaining to asymmetric spreading. We did this because, for the purposes of our analysis, we were interested only in the total amount of new seafloor generated. We then took the product of the spreading segment length and full spreading rate to calculate the seafloor production rate (in km^2 Myr^{-1}) and then summed the area of all segments per time step to obtain a total seafloor production per Myr (equation (1)), as follows:

$$SP(t) = \sum_j uL \qquad (1)$$

Geochemical analysis of the volcanic tuffs. We carried out major, trace and isotopic analysis (variously) on 20 tuff layers sampled from Deep Sea Drilling Project (DSDP) Site 555 on the Rockall Plateau. X-ray fluorescence analyses were carried out in the Grant Institute of Earth Science at the University of Edinburgh, using procedures described in refs. [62,63]. Major-element concentrations (Extended Data Table 1) were determined after fusion with a lithium borate flux containing La_2O_3 as a heavy absorber, using an existing method[64]. Rock powder was dried at 110 °C for at least 1 h, and a precisely weighed 1 g aliquot ignited at 1,100 °C to determine loss on ignition. The residue was then mixed with Johnson Matthey Spectroflux™ 105 in a sample:flux ratio of 1:5, based on the unignited sample mass, and fused in a muffle furnace in a Pt5%Au crucible. After the initial fusion, the crucible was reweighed, and any flux weight loss was made up with extra flux. After a second fusion over a Meker burner, the molten mixture was swirled several times to ensure homogeneity, cast onto a graphite mould and flattened with an aluminium plunger into a thin disk. The mould and plunger were maintained at a temperature of 220 °C on a hot plate.

Trace element concentrations (Extended Data Table 1) were determined on pressed-powder samples. Eight grams of rock powder were mixed thoroughly with eight drops of a 2% aqueous solution of polyvinyl alcohol. The mixture was loaded into a 40 mm-diameter aluminium cup in a stainless-steel die and compressed against a polished tungsten carbide disc in a hydraulic press at 0.6 tons cm^{-2}. The fused and pressed samples were analysed using a PANalytical PW 2404 automatic X-ray fluorescence spectrometer with a Rh-anode X-ray tube. Trace element background positions were placed as close as possible to peaks, and long count times were used at both peak and background positions. Where background count rates were measured on either side of the peak, as in most trace element determinations, the count time was divided between the two positions. Analytical conditions are given in refs. [62,63].

Corrections for matrix effects on the intensities of major-element lines were made using theoretical alpha coefficients calculated online using the PANalytical software. The coefficients were calculated to allow for the amount of extra flux replacing volatile components in the sample so that analytical totals should be 100% less than the measured loss on ignition. Intensities of the longer wavelength trace element lines (La, Ce, Nd, Cu, Ni, Co, Cr, V, Ba and Sc) were corrected for matrix effects using alpha coefficients based on major-element concentrations measured at the same time on the powder samples. Matrix corrections were applied to the intensities of the other trace element lines by using the count rate from the RhK$_\alpha$ Compton scatter line as an internal standard[65]. Line-overlap corrections were applied using synthetic standards.

The spectrometer was calibrated against U.S. Geological Survey (USGS) and Centre de Recherches Pétrographiques et Géochimiques (CRPG) geochemical reference standards using the values given by Govindaraju (1994)[66], except that the values of Jochum et al. (1990)[67] were used for Nb and Zr in BCR-1 and BHVO-1. Excellent calibration lines were obtained using these standards. Analytical precision and accuracy are comparable to the values reported in refs. [62,63]. Four USGS geostandards were analysed along with the samples and the data from these (Supplementary Table 1) were used to assess accuracy and precision.

Trace element analysis was performed on a representative selection of four of the tuffs using an Inductively Coupled Plasma Mass Spectrometer (ICP-MS). Samples were homogenized using a unidirectional crushing machine before dissolution via a three-stage, mixed acid (HF-HNO_3-HCl) closed-vessel approach. After digestion, samples were dried down before resuspension in 2% HNO_3 for analysis, carried out using a Thermo Scientific X-Series-2 at the University of Southampton. Alongside samples (Extended Data Table 3), blanks and International standard JA-2 (ref. [68]) and Southampton internal basalt standard BRR-1 (ref. [69]) were prepared and analysed; recoveries of JA-2 and BRR-1 are shown in Supplementary Table 2.

Finally, we analysed the $^{143}Nd/^{144}Nd$ isotope composition of several samples of tuff from Site 555 (Fig. 2a and Extended Data Table 2). Here ~25 mg of freeze-dried sediment was homogenized using a pestle and mortar before leaching in 6M HCl for 2 h to remove any diagenetic, alteration-related material. Samples were then digested via a mixed acid, closed-vessel HNO_3-HF approach on a hot plate at 120 °C. Digests were then taken to incipient dryness before resuspension in 2% HNO_3 for analysis. All acids were sub-boiled to ensure purity and prepared at the University of Southampton. Aliquots were then purified via first cation (AG50-X8 200–400 mesh resin) and then reverse phase (LN Spec, Eichrom Industries) chromatography to remove isobaric interferents. All measurements were made on a Thermo Fisher Neptune Multi-Collector-ICP-MS at the University of Southampton. Mass bias corrections were performed using repeat measurements of the standard JNdi-1 (ref. [70]) with a $^{143}Nd/^{144}Nd$ value of 0.512115. Nd isotope ratios are presented using epsilon notation as follows:

$$\epsilon Nd = \left(\frac{^{143}Nd/^{144}Nd_{sample}}{^{143}Nd/^{144}Nd_{CHUR}} - 1 \right) \times 10^4 \qquad (2)$$

where $^{143}Nd/^{144}Nd_{CHUR}$ is the Nd isotopic composition of the chondrite uniform reservoir, with a value of 0.512638 (ref. [71]). Repeat analysis of two separately digested JNdi-1 samples ($n=8$, two standard deviations [2SD]) yielded $^{143}Nd/^{144}Nd$ accuracy and precision values of 0.5121124 ± 0.000006, corresponding to ϵNd of 10.25 ± 0.12. This is in close agreement with literature values of 0.512115 ± 0.000007 (ref. [70]). Procedural blanks were between 45 pg and 50 pg Nd, comprising < 1% of the sample Nd in all cases. Present day ϵNd values were corrected for radioactive ingrowth from ^{147}Sm following its formation using a radioactive decay constant for ^{147}Sm of 6.54×10^{-12} years, a sample age of 55 Ma and the ratio of $^{147}Sm/^{144}Nd$ as measured in pre-column chemistry solutions.

Establishing a chronostratigraphic framework. We established a chronostratigraphic framework for Site 555 on the Rockall Plateau, building on several existing constraints at this site (Fig. 1a). The PETM as geochemically defined could not be identified at this site because of the high proportion of volcanic and siliciclastic material (Fig. 2a), intruded at many levels by dolerite dykes and sills with emplacement temperatures likely in the range ~1,000 °C to 1,250 °C. Thus, the adjacent sediments probably experienced temperatures >650 °C, thermal conditions which are known to seriously affect $\delta^{13}C$ composition in mudrocks and carbonates[72]. Accordingly, we rely on a combination of radiometric, magnetostratigraphic and palaeontological age constraints, in addition to well-defined sediment accumulation rate estimates. The most reliable radiometric date in this sequence, from an olivine phyric basalt near the Palaeocene–Eocene boundary, yielded a K–Ar age of 54.5 ± 2 Ma (ref. [73]). Although uncertain, this can be narrowed further by considering the distribution of calcareous nannoplankton, including *Fasciculithus*, which disappears in the mudstones below the hyaloclastites (top NP9), with its last occurrence dated to ~55.6 Ma (http://www.mikrotax.org). This suggests that the age of the lava is most likely in the range 56.5–55.6 Ma, supporting the original position of the Palaeocene–Eocene boundary[74]. Further, the overlying mudstones interbedded with the tuffs are thought to contain the dinoflagellate cyst species, *Apectodinium augustum*[20], characteristic of the TP5a palynozone[75]. Therefore, most of the tuff layers at Site 555 (Fig. 2) were emplaced before and during the PETM. We estimate the duration of this eruptive phase by calculating the thickness of strata between the bottom and upper tuffs in the phase (that is, 691 and 605.5 m below sea level, respectively) and using the sediment accumulation rates (50 cm kyr^{-1}) at these levels at Site 555 (ref. [22]). This gives a duration of 171 kyr, which is near identical to that of the contemporaneous PETM interval[8,12]. However, given that the earliest tuffs occur just below the Palaeocene–Eocene boundary, the true duration is more likely to be of the order of 213 kyr, assuming that the PETM section represents the 170 kyr interval[8,12]. This interpretation is consistent with the occurrence of tuffs in the upper part of the sequence (Extended Data Figs. 1 and 3) that are geochemically similar to those reported in the PETM recovery phase elsewhere in the NAIP[22]. We therefore consider a duration range of 171–213 kyr to be most reasonable for this eruptive phase. Given the above observations, we estimate the age of basal strata in this hole (~950 m) at 56.6 Ma, which is consistent with biostratigraphy and magnetostratigraphy[22].

The base of the Milne Land Formation (Lower), which is correlated with the base of the Faroes Middle Lava Formation[1,26] has been well-dated at 56.1 ± 0.4 Ma. Storey et al. (2007)[1] use the relative age of the well-dated Danish Ash-17 to firmly place the PETM interval after the onset of Middle Lavas volcanism. A late Palaeocene age is also supported by palynologic studies of the underlying (non-marine) coal-bearing Prestfjall Formation and its position near the boundary between magnetic polarity chrons c24r and c25n[76] (that is, 57.1 Ma (ref. [77])). For the Upper Lava Formation, we assumed an upper age of 55.5 Ma; this is based on an average of three radiometric ages, including one obtained from the uppermost Upper Lava Formation in the Faroes (55.1 ± 0.5 Ma (ref. [1])). We used two radiometric ages obtained from the Skaergaard intrusion (55.75 ± 0.3 Ma, and 55.65 ± 0.3 Ma (ref. [78])), where the parental magma has been genetically linked to the Milne Land Formation[79], and accordingly, its crystallization is considered to provide an upper age constraint for Milne Land Formation volcanism[1]

(and thus, the lower Geikie Plateau Formation[26]). Using this age model, we calculate the duration of the lowermost high-Mg# part of the Middle Lavas (that is, the lowermost 800 m; Fig. 2b) to be 227 kyr, similar to that of the volcanic phase at Rockall.

Establishing a chronostratigraphic framework for the Faroese Lower Lava Formation (correlative with the Nansen Fjord Formation of eastern Greenland) is more challenging because of the large uncertainties associated with radiometric ages through this succession[2]. However, this inherent uncertainty does not impact our results in any way; data for the lower formations are shown only for reference purposes on our stratigraphic section (Fig. 2b,c). As a reasonable solution, we used magnetic polarity chrons for the Faroes sequence[80], combined with the chemical stratigraphy of Larsen et al. (1999)[26] and using a standard geomagnetic polarity time scale[77]. We calibrated the ages at certain depths in the succession using the ages of chron boundaries as tie points and applying a linear interpolation between these known points (which assumes constant lava accumulation rates). We found that this age model was broadly consistent with existing radiometric ages (that is, in most cases within uncertainty)[2].

Rare earth element melting model. A simple batch melting equation was used in the construction of Fig. 2e:

$$C_L/C_0 = \frac{1}{D + F - PF} \qquad (3)$$

where C_0 is the initial concentration of some element in the mantle source, C_L is its concentrations in the liquid, F is the melt fraction, D is the average distribution coefficient for the mantle phases weighted by their respective mass fractions before the onset of melting and P is the average distribution coefficient for the mantle phases weighted by their respective contribution to the melt (see ref. [81]). We use a peridotite mantle source with a mineralogical composition given by McKenzie and O'Nions (1991)[82]: (1) 57.8% olivine, 27.0% orthopyroxene, 11.9% clinopyroxene and 3.3% spinel (spinel lherzolite) and (2) 59.8% olivine, 21.1% orthopyroxene, 7.6% clinopyroxene and 11.5% garnet (garnet lherzolite). Partition coefficients (D) vary considerably with pressure, temperature and liquid composition, and this limits the reliability of partial melting models because the choice of values is always somewhat subjective. Here we have attempted to be more objective by using averages of all appropriate published D values (Extended Data Table 4). We use the following mantle melting proportions for spinel lherzolite (equation (4); ref. [83]) and garnet lherzolite (equation (5); ref. [84]):

$$\text{liquid} = -0.22 \, \text{ol} + 0.38 \, \text{opx} + 0.71 \, \text{cpx} + 0.13 \, \text{sp} \qquad (4)$$

$$\text{liquid} = 0.08 \, \text{ol} - 0.19 \, \text{opx} + 0.81 \, \text{cpx} + 0.30 \, \text{gt} \qquad (5)$$

where ol is olivine, opx is orthopyroxene, sp is spinel, cpx is clinopyroxene and gt is garnet.

The concentrations of rare earth elements in our mantle source (Ce 1.236 ppm, Sm 0.346 ppm, Yb 0.432 ppm) are calculated from the composition of primitive basalt from the Ontong Java Plateau and are thought to be typical of mantle plumes[85].

Please note that Extended Data Table 4 cites additional references[86–93].

Modelling of CO_2 fluxes. We perform a simple Monte Carlo simulation, sampling from probability distributions for six uncertain parameters (Extended Data Tables 5 and 6) to estimate the probable combined CO_2 emissions from incipient ridge volcanism and active LIPs. This enables us to evaluate the relative contributions to carbon release during the PETM due to ridge production and LIP formation. We also calculate the effect of incorporating carbonated SCLM melt in different amounts during enhanced melting along the incipient ridge axis. In our calculations, we assumed a PETM duration of 170 kyr (refs. [8,12]). We use Beta distributions to represent uncertainty in the parameters (Extended Data Table 6). The Beta distribution is a continuous distribution over a fixed interval [0, 1] but can be re-scaled to any desired range. It is defined by two shape parameters α and β, which can be estimated from the distribution mean (μ) and variance (σ^2):

$$\alpha = \mu \left(\mu \, \frac{(1 - \mu)}{\sigma^2} - 1 \right) \qquad (6)$$

$$\beta = \alpha \left(\frac{1}{\mu} - 1 \right) \qquad (7)$$

where μ is the mean, σ is standard deviation and σ^2 is the variance. To estimate Beta distribution parameters, we use best estimates (from published data and observations) of the minimum, mean and maximum values for each variable (Extended Data Table 6 and discussed below) and apply these to equations (6) and (7) above (using re-scaled values for μ and σ). For simplicity, we assume that the standard deviation for a given variable is 20% of the range, $\sigma_v = 0.2$ (max–min). The inputs to the calculations (sampled, constant and fixed) and outputs are listed in

Extended Data Tables 5 and 6, and the corresponding histograms for each of the sampled variables are shown in Extended Data Fig. 4.

To quantify the CO_2 degassing flux from ridges in the NAIP (that is, the northeast Atlantic and the Labrador Sea), we used seafloor production rates parameterized from plate tectonic reconstructions (see above) for the ridges at 55 Ma—the first time step at which seafloor generation is recorded in the northeast Atlantic. In these calculations, we assumed an oceanic crustal thickness of 6 km, the global average[94]. Only a small fraction of the total amount of CO_2 available in the basaltic oceanic crust is degassed at ridges. To estimate this, we used the ratio between the oceanic crustal productivity (that is, the total amount of crust formed, which is ~18 km³ per year) and the estimated CO_2 fluxes from the present day global ridge system (7×10^{11} mol per year; a middle value of ref. [18]). This analysis indicates that about 10% of the CO_2 available in the ocean crust is degassed at ridges (see main text), mostly corresponding to the upper 600 m. Thus, in our simulations we used a Beta distribution with a mean value of 10% (that is, 10% of the total available CO_2 is lost from the crust) and minimum and maximum values of 5% and 15%, respectively. For the pre-eruptive CO_2 content of basaltic magmas, we used a Beta distribution with a mean value of 0.5 wt%, and minimum and maximum values of 0.2 wt% and 2 wt%, considered reasonable for flood basalts[17] and ocean crust at this time[95]. To estimate the CO_2 fluxes from LIPs, we used existing eruptive rate estimates for the NAIP[4]. We consider two LIP eruptive rate scenarios: (S1) low flood basalt productivity (0.6 km³ per year) and (S2) high productivity (2.4 km³ per year[9]). The combined fluxes from incipient ridge volcanism and each of these eruptive scenarios for LIPs are shown as the grey lines on our cumulative distribution functions (Fig. 3). We assumed near-total loss of CO_2 from flood basalt volcanism (mean 95%, minimum 90%, maximum 100% loss) based on observations from fresh basaltic glass in flood basalts that show most of the CO_2 is lost to degassing[17]. Ridge and LIP CO_2 outgassing was calculated using equation (8):

$$W_{CO\text{ocean}} = \frac{12}{44} \frac{t_{\text{rift}}}{10^{12}} \left(O_{\text{Floss}} r_{\text{basaltprod}} \rho_{\text{basalt}} B_{\text{FractCO}_2} \right) + \left(C_{\text{FractLIP}} r_{\text{LIPprod}} \rho_{\text{basalt}} B_{\text{FractCO}_2} \right) \qquad (8)$$

where $W_{CO\text{ocean}}$ is total weight of C released from the ocean crust and LIPs; t_{rift} is the duration of extension in years; O_{Floss} is the fraction of CO_2 lost from the ocean crust; $r_{\text{basaltprod}}$ is volumetric rate of basalt production from the NAIP ridges (equation (1)); ρ_{basalt} is density of basalt (3,000 kg m^{-3}); B_{FractCO_2} is CO_2 content (weight percent) of basalt, expressed as a fraction; C_{FractLIP} is the fraction of LIPs that are fully degassed of CO_2; and r_{LIPprod} is the volumetric rate of basalt production from LIPs. Note that a factor of 12/44 converts from mass of CO_2 to mass of C.

The combined carbon flux estimates show that outgassing from ridges and LIPs alone are insufficient to trigger PETM warming, unless they are augmented by a transient increase in CO_2 content (as we propose via the incorporation of carbonated SCLM during mantle melting). To account for this apparent deficit, we estimated the potential influence of SCLM melting contributions, using scenarios S1 and S2 (above) as a baseline (that is, the background volcanic carbon flux; Fig. 3). During continental extension (as in the early Cenozoic northeast Atlantic), the deep metasomatized lithospheric mantle is stretched along the length of the rift[39] (Fig. 4). The lithospheric extension raises the cratonic lithosphere, exposing metastable metasomatized domains to anomalously hot asthenospheric melts upwelling beneath the rift axis. This process is expected to occur along the length of the evolving rift. We estimated the total volume of carbonated SCLM (c-SCLM) from the length of the rift segments active between 56–55 Ma (Fig. 1d), assuming a plausible range of thicknesses and melting widths for this layer (Extended Data Table 6).

The precise thickness of the c-SCLM of the North Atlantic craton at 55 Ma is poorly constrained and is likely to have been spatially heterogeneous but is considered to lie in the range of 10 km (ref. [43]) to ~30 km thick (based on chemical tomography of cratonic regions[96]), which is broadly consistent with geochemical and tectono–magmatic models of the North Atlantic craton[97,98]. We assume a mean c-SCLM thickness of 20 km, with minimum and maximum values of 5 km and 25 km. We estimated the width of SCLM involved in melting using petrological–thermomechanical models of lithospheric rifting processes[43]. In cases where the lithosphere is about 200 km thick, the width of the melting zone is most likely to be of the order of 25 km (ref. [43]). We therefore used a Beta distribution with a mean width of 25 km and range of 5 km to 30 km. Melting of metasomatic material occurs on both sides of the stretching lithosphere, doubling the total contribution to CO_2 output. c-SCLM is expected to have a high CO_2 content, of the order 5–8 wt%, but potentially even higher[41]. We therefore use a mean value of 5 wt%, minimum of 1 wt% and maximum of 10 wt%. The total contribution of SCLM melting to fluxes was estimated using equation (9):

$$W_{\text{CSCLM}} = \frac{l_{\text{SCLM}} w_{\text{SCLM}} h_{\text{SCLM}} \rho_{\text{SCLM}}}{10^{12}} \qquad (9)$$

where W_{CSCLM} is total weight of carbon in the SCLM (Gt); l_{SCLM} is the length of SCLM involved in melting along the northeast Atlantic rift system; w_{SCLM} is the width of the SCLM zone (km); h_{SCLM} is thickness of the SCLM (km) and ρ_{SCLM} is density of SCLM (lherzolite; 3,200 kg m^{-3}). A factor of 1/10^{12} converts weight from

kg to Gt. Finally, we calculated the total weight of carbon (W_{TotalC}) produced from the ocean crust, LIPs and enhanced melting of the c-SCLM using equation (10):

$$W_{TotalC} = W_{COcean} + F_{CSCLM}W_{CSCLM} \qquad (10)$$

where F_{CSCLM} is the fraction of c-SCLM melted during extension (calculated with 0.04, 0.05 and 0.08; see Fig. 3).

Please note that additional references are cited in the Extended Data figures and tables[99–105].

Data availability

All data generated or analysed during this study are provided in the online version of this article (Supplementary Data File S1) and in Extended Data Tables 1–6. The map in Fig. 1b was plotted with open source plate tectonic application software GPlates (https://www.gplates.org/; licensed for distribution under a GNU General Public License). Any new geochemical data generated in this study are also available to download via the figshare repository at: https://doi.org/10.6084/m9.figshare.19732948. Source data are provided with this paper.

Code availability

More details on the computational methods and tools used for this study are available from the corresponding author upon reasonable request.

References

57. Müller, R. D. et al. Ocean basin evolution and global-scale plate reorganization events since Pangea breakup. *Ann. Rev. Earth Planet. Sci.* **44**, 107–138 (2016).
58. Karlsen, K. S., Conrad, C. P. & Magni, V. Deep water cycling and sea level change since the breakup of Pangea. *Geochem. Geophys. Geosyst.* **20**, 2919–2935 (2019).
59. Karlsen, K. S., Domeier, M., Gaina, C. & Conrad, C. P. A tracer-based algorithm for automatic generation of seafloor age grids from plate tectonic reconstructions. *Comput. Geosci.* **140**, 104508 (2020).
60. Merdith, A. S., Atkins, S. E. & Tetley, M. G. Tectonic controls on carbon and serpentinite storage in subducted upper oceanic lithosphere for the past 320 Ma. *Front. Earth Sci.* **7**, 332 (2019).
61. Merdith, A. S. et al. Pulsated global hydrogen and methane flux at mid-ocean ridges driven by Pangea breakup. *Geochem. Geophys. Geosyst.* **21**, e2019GC008869 (2020).
62. Fitton, J., Saunders, A., Larsen, L., Hardarson, B. & Norry, M. Volcanic rocks from the southeast Greenland Margin at 63°N: composition, petrogenesis, and mantle sources. *Proc. Ocean Drill. Prog. Sci. Results* **152**, 331–350 (1998).
63. Fitton, J. G. & Godard, M. Origin and evolution of magmas on the Ontong Java Plateau. *Geol. Soc. Spec. Publ.* **229**, 151–178 (2004).
64. Norrish, K. & Hutton, J. T. An accurate X-ray spectrographic method for the analysis of a wide range of geological samples. *Geochim. Cosmochim. Acta* **33**, 431–453 (1969).
65. Reynolds, R. C. Matrix corrections in trace element analysis by X-ray fluorescence: estimation of the mass absorption coefficient by Compton scattering. *Am. Mineral.* **48**, 1133–1143 (1963).
66. Govindaraju, K. 1994 compilation of working values and sample description for 383 geostandards. *Geostand. Newsl.* **18**, 1–158 (1994).
67. Jochum, K. P., Seufert, H. M. & Thirlwall, M. F. High-sensitivity Nb analysis by spark-source mass spectrometry (SSMS) and calibration of XRF Nb and Zr. *Chem. Geol.* **81**, 1–16 (1990).
68. Imai, N., Terashima, S., Itoh, S. & Ando, A. 1994 compilation of analytical data for minor and trace elements in seventeen GSJ geochemical reference samples, "igneous rock series". *Geostand. Newsl.* **19**, 135–213 (1995).
69. Murton, B. J., Taylor, R. N. & Thirlwall, M. F. Plume–ridge interaction: a geochemical perspective from the Reykjanes Ridge. *J. Petrol.* **43**, 1987–2012 (2002).
70. Tanaka, T. et al. JNdi-1: a neodymium isotopic reference in consistency with LaJolla neodymium. *Chem. Geol.* **168**, 279–281 (2000).
71. Jacobsen, S. B. & Wasserburg, G. J. Sm–Nd isotopic evolution of chondrites. *Earth Planet. Sci. Lett.* **50**, 139–155 (1980).
72. Munro, L. E., Longstaffe, F. J. & White, C. D. Effects of heating on the carbon and oxygen-isotope compositions of structural carbonate in bioapatite from modern deer bone. *Palaeogeogr. Palaeoclimatol. Palaeoecol.* **266**, 142–150 (2008).
73. Macintyre, R. M. & Hamilton, P. J. in *Initial Reports DSDP* Vol. 81 (eds Roberts, D. G. et al.) Ch. 30 (US Government Printing Office, 1984).
74. Roberts, D. G., Backman, J. Morton, A. C., Murray, J. W. & Keene, J. B. in *Initial Reports DSDP* Vol. 81 (eds Roberts, D. G. et al.) Ch. 39 (US Government Printing Office, 1984).
75. Berggren, W. A., Kent, D. V., Swisher, C. C. & Aubrey, M. P. A revised Cenozoic geochronology and chronostratigraphy. *Soc. Sediment. Geol. Spec. Publ.* **54**, 129–212 (1995).
76. Lund, J. A late Paleocene non-marine microflora from the interbasaltic coals of the Faeroe Islands, North Atlantic. *Bull. Geol. Soc. Denmark* **37**, 181–203 (1988).
77. J. G., Ogg. in *Geomagnetic Polarity Time Scale*. Ch. 5 (Elsevier, 2012).
78. Hirschmann, M. M., Renne, P. R. & McBirney, A. R. ^{40}Ar/^{39}Ar dating of the Skaergaard intrusion. *Earth Planet. Sci. Lett.* **146**, 645–658 (1997).
79. Jakobsen, J. K. et al. Parental magma of the Skaergaard intrusion: constraints from melt inclusions in primitive troctolite blocks and FG-1 dykes. *Contrib. Mineral. Petrol.* **159**, 61–79 (2009).
80. Waagstein, R. Structure, composition and age of the Faeroe basalt plateau. *Geol. Soc. Spec. Publ.* **39**, 225–238 (1988).
81. Fitton, J. G., Williams, R., Barry, T. L. & Saunders, A. D. The role of lithosphere thickness in the formation of ocean islands and seamounts: contrasts between the Louisville and Emperor–Hawaiian hotspot trails. *J. Petrol.* **61**, egaa111 (2020).
82. McKenzie, D. & O'Nions, R. K. Partial melt distributions from inversion of rare earth element concentrations. *J. Petrol.* **32**, 1021–1091 (1991).
83. Baker, M. B. & Stolper, E. M. Determining the composition of high-pressure mantle melts using diamond aggregates. *Geochim. Cosmochim. Acta* **58**, 2811–2827 (1994).
84. Walter, M. J. Melting of garnet peridotite and the origin of komatiite and depleted lithosphere. *J. Petrol.* **39**, 29–60 (1998).
85. Hastie, A. R. et al. The composition of mantle plumes and the deep earth. *Earth Planet. Sci. Lett.* **444**, 13–25 (2016).
86. Hart, S. R. & Dunn, T. Experimental cpx/melt partitioning of 24 trace elements. *Contrib. Mineral. Petrol.* **113**, 1–8 (1993).
87. Hauri, E. H., Wagner, T. P. & Grove, T. L. Experimental and natural partitioning of Th, U, Pb and other trace elements between garnet, clinopyroxene and basaltic melts. *Chem. Geol.* **117**, 149–166 (1994).
88. Johnson, K. T. M. Experimental determination of partition coefficients for rare earth and high-field-strength elements between clinopyroxene, garnet, and basaltic melt at high pressures. *Contrib. Mineral. Petrol.* **133**, 60–68 (1998).
89. McDade, P., Blundy, J. D. & Wood, B. J. Trace element partitioning on the Tinaquillo Lherzolite solidus at 1.5 GPa. *Phys. Earth Planet. Int.* **139**, 129–147 (2003).
90. Salters, V. J. M., Longhi, J. E. & Bizimis, M. Near mantle solidus trace element partitioning at pressures up to 3.4 GPa. *Geochem. Geophys. Geosyst.* **3**, 1–23 (2002).
91. Skulski, T., Minarik, W. & Watson, E. B. High-pressure experimental trace-element partitioning between clinopyroxene and basaltic melts. *Chem. Geol.* **117**, 127–147 (1994).
92. Tuff, J. & Gibson, S. A. Trace-element partitioning between garnet, clinopyroxene and Fe-rich picritic melts at 3 to 7 GPa. *Contrib. Mineral. Petrol.* **153**, 369–387 (2007).
93. Irving, A. J. A review of experimental studies of crystal/liquid trace element partitioning. *Geochim. Cosmochim. Acta* **42**, 743–770 (1978).
94. Perfit, M. R. in *Encyclopedia of Ocean Sciences* 2nd edn (ed. Steele, J. H.) 815–825 (Academic Press, 2001).
95. Müller, R. D. & Dutkiewicz, A. Oceanic crustal carbon cycle drives 26-million-year atmospheric carbon dioxide periodicities. *Sci. Adv.* **4**, eaaq0500 (2018).
96. O'Reilly, S. Y. & Griffin, W. L. Imaging global chemical and thermal heterogeneity in the subcontinental lithospheric mantle with garnets and xenoliths: geophysical implications. *Tectonophysics* **416**, 289–309 (2006).
97. Tappe, S. et al. Craton reactivation on the Labrador Sea margins: ^{40}Ar/^{39}Ar age and Sr–Nd–Hf–Pb isotope constraints from alkaline and carbonatite intrusives. *Earth Planet. Sci. Lett.* **256**, 433–454 (2007).
98. Tappe, S. et al. Sources and mobility of carbonate melts beneath cratons, with implications for deep carbon cycling, metasomatism and rift initiation. *Earth Planet. Scie. Lett.* **466**, 152–167 (2017).
99. Harrison, R. K. and Merriman, R. J. in *Initial Reports DSDP* Vol. 81 (eds Roberts, D. G. et al.) Ch. 29 (US Government Printing Office, 1984).
100. Gernon, T. M. et al. Complex subvolcanic magma plumbing system of an alkali basaltic maar–diatreme volcano (Elie Ness, Fife, Scotland). *Lithos* **264**, 70–85 (2016).
101. Le Bas, M. J., Le Maitre, R. W., Streckeisen, A. & Zanettin, B. A chemical classification of volcanic rocks based on the total alkali–silica diagram. *J. Petrol.* **27**, 745–750 (1986).
102. Chambers, L. M. *Age and Duration of the British Tertiary Igneous Province: Implications for the Development of the Ancestral Iceland Plume.* PhD thesis, Univ. of Edinburgh (2000).
103. Brodie, J. A. & Fitton, J. G. Data report: composition of basaltic lavas from the seaward-dipping reflector sequence recovered during Deep Sea Drilling Project Leg 81 (Hatton Bank). *Proc. Ocean Drill. Prog. Sci. Res.* **152**, 431–435 (1998).
104. Fitton, J. G., Mahoney, J. J., Wallace, P. J. & Saunders, A. D. Origin and evolution of the Ontong Java Plateau: introduction. *Geol. Soc. Spec. Publ.* **229**, 1–8 (2004).

105. McDonough, W. F. & s. Sun, S. The composition of the Earth. *Chem. Geol.* **120**, 223–253 (1995).

Acknowledgements

Author contributions

T.M.G. conceived the idea, led the study, interpreted the data and prepared the manuscript and figures. T.K.H. performed the modelling, with input from T.M.G. R.N.M. assisted with tectonic and geodynamic interpretation, and J.G.F., J.L., R.B. and M.R.P. provided support with geochemical analysis and interpretation. J.G.F. carried out the melt modelling with input from T.M.G. A.S.M. calculated the seafloor production rates and provided support with GPlates and 'pyGPlates'. D.K. contributed to tectonic interpretations. T.M.G. wrote the manuscript with input from all co-authors.

Competing interests

The authors declare no competing interests.

Additional information

Extended data is available for this paper at https://doi.org/10.1038/s41561-022-00967-6.

Supplementary information The online version contains supplementary material available at https://doi.org/10.1038/s41561-022-00967-6.

Correspondence and requests for materials should be addressed to Thomas M. Gernon.

Peer review information Primary Handling Editors: James Super and Rebecca Neely, in collaboration with the *Nature Geoscience* team. *Nature Geoscience* thanks James Muirhead, Sverre Planke and the other, anonymous, reviewer(s) for their contribution to the peer review of this work.

Reprints and permissions information is available at www.nature.com/reprints.
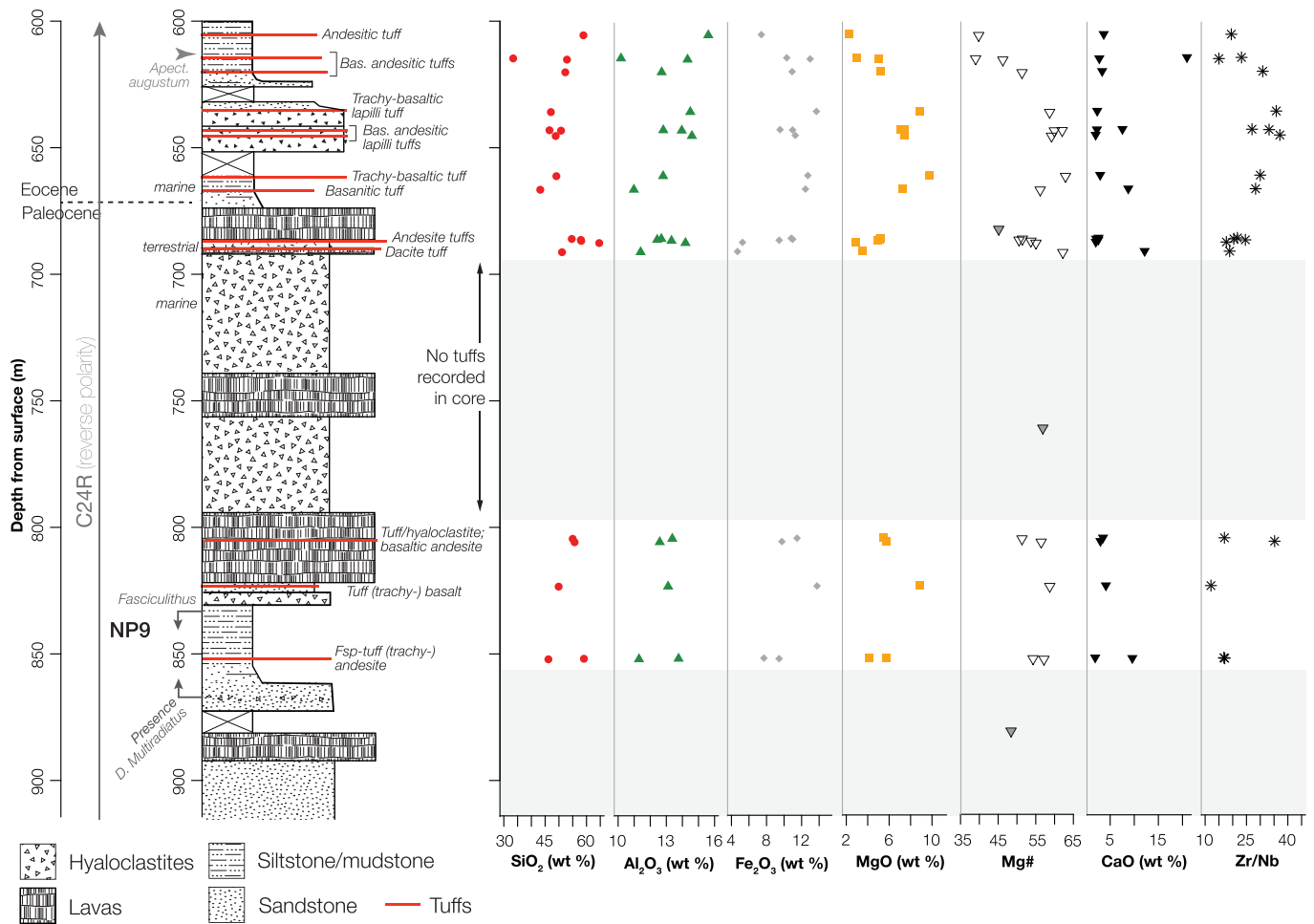
Extended Data Fig. 1 | Schematic stratigraphic log of Palaeocene–Eocene volcanic and sedimentary lithofacies at DSDP Leg 81 Site 555, and the composition of tuff layers. The corresponding plots show the major-element composition, and Mg#, of tuff layers, shown as horizontal red lines (and labelled by lithology; see also Extended Data Fig. 3a) on the log. The Mg# of a number of basalt lavas and tuffs from Harrison and Merriman[99] are also shown as filled grey symbols.
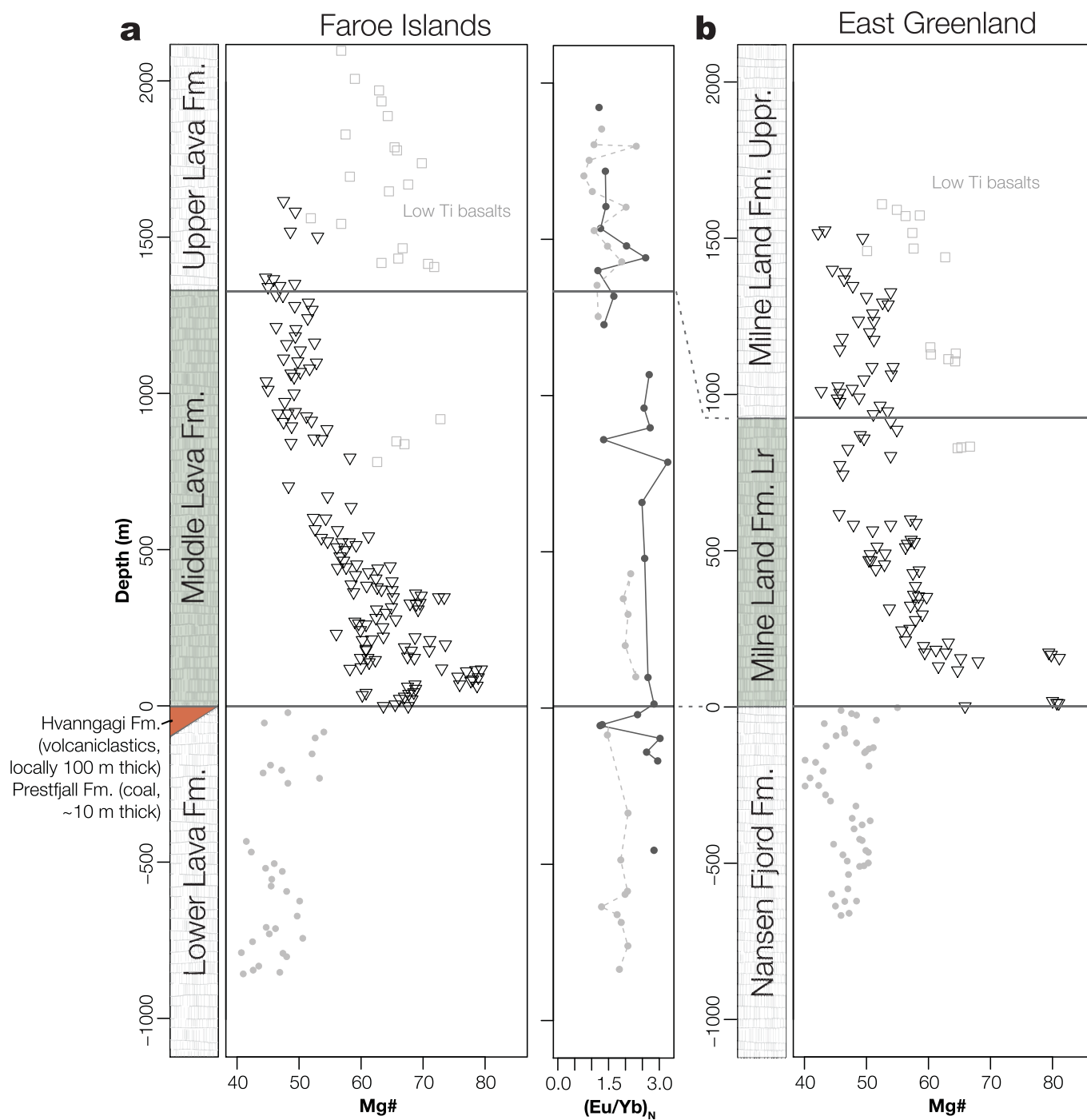
Extended Data Fig. 2 | Compositional characteristics of lavas from the Faroes and Greenland. Simplified log of basalt lava successions from the Faroes and east Greenland (modified after ref. [26], with Mg# and $(Eu/Yb)_n$ (chondrite-normalised[56]); Mg# data are from ref. [26] and $(Eu/Yb)_n$ are from refs. [27,32].
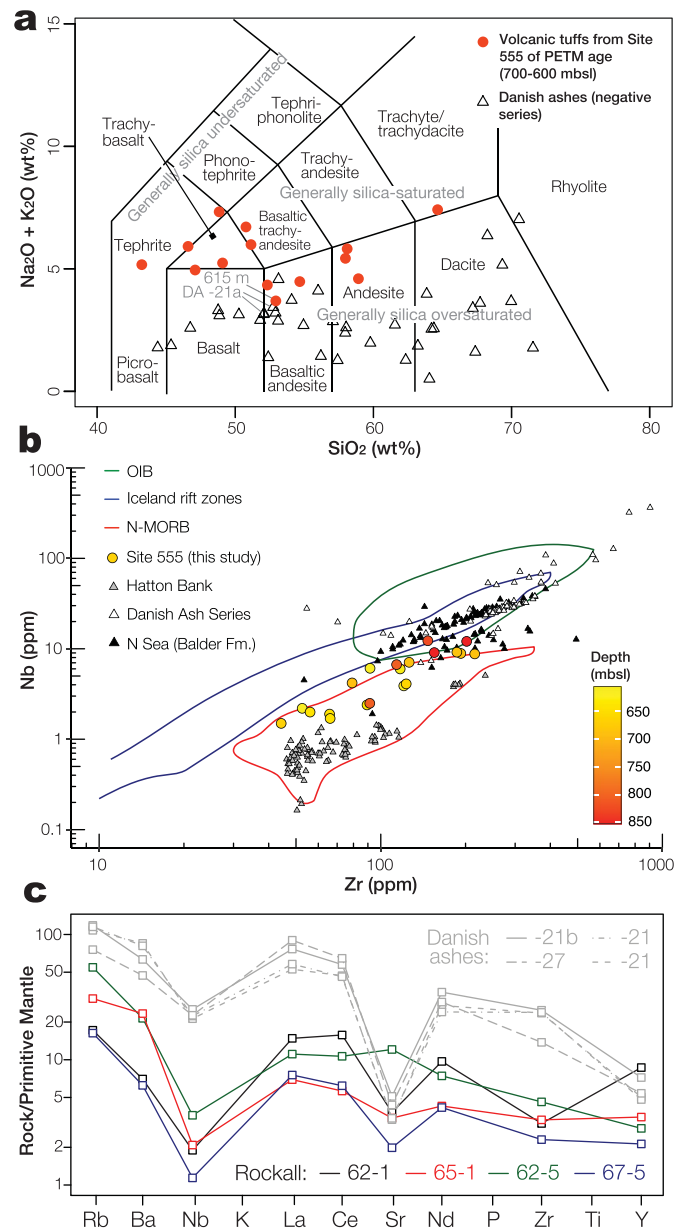
Extended Data Fig. 3 | Geochemical characteristics of tuffs layers from DSDP Leg 81 Site 555. Total alkali-silica (TAS) diagram (after ref. [101]) showing the composition of volcanic tuffs of PETM age (approximately 700-600 mbsl; see Extended Data Fig. 2), in addition to Danish ashes of the 'negative series'[23]. b, Nb versus Zr of tuffs from Site 555, shown alongside tuffs of the Danish Ash Series[23] and Balder Formation in the North Sea[102], and lavas from the Rockall/Hatton Bank[103]. The fields shown for OIB, N-MORB and Iceland rift-zones are from ref. [104]. c, Incompatible element patterns of Rockall tuffs from the upper section (700-600 mbsl) normalized to primitive mantle[105]. The corresponding depths in the core are provided in Extended Data Table 3. For comparison, some Danish ashes (negative series) are also shown[23].
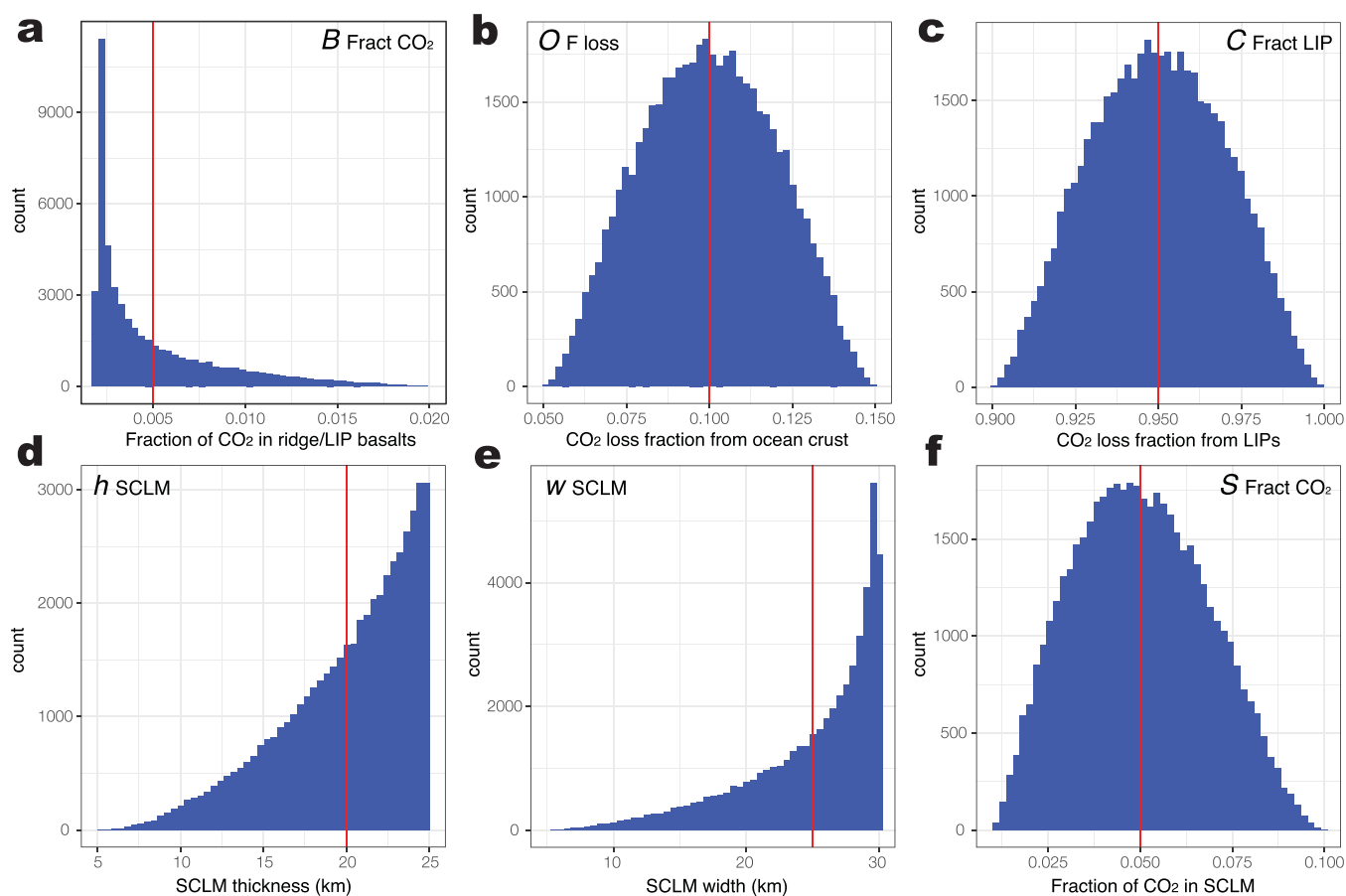
Extended Data Fig. 4 | Input distributions for sampled variables used in carbon outgassing simulations. a, Fraction of CO_2 present in mid-ocean ridge basalts and those of large igneous provinces (LIPs); b, Fraction of CO_2 lost from the ocean crust via degassing at mid-ocean ridges; c, Fraction of CO_2 lost from LIP basalt eruptions; d, Thickness of the sub-continental lithospheric mantle (SCLM); e, Width of the SCLM melting zone beneath the mid-ocean ridge system; f, Fraction of CO_2 present in the SCLM. Note that the red line denotes the mean. See the Methods for further information on these variables.

Sample name	TG1	TG2	TG3	TG4	TG5	TG6	TGT-01	TGT-02	TGT-03	TGT-04	TGT-05	TGT-06	TGT-07	TGT-08	TGT-09	TGT-10	TGT-11	TGT-12	TGT-13	TGT-14
DSDP core site	555	555	555	555	555	555	555	555	555	555	555	555	555	555	555	555	555	555	555	555
Sample depth (mbsl)	614.69	620.17	643.07	666.58	804.5	852.1	605.55	615.15	635.88	643.22	645.34	661.2	686.01	686.39	686.77	687.63	691.25	805.84	823.28	851.88
Major elements (wt.%)																				
SiO_2	33.40	52.31	46.57	43.23	55.00	46.18	58.89	52.92	47.08	50.76	48.82	49.07	54.65	57.95	58.08	64.62	51.12	55.68	49.90	59.07
Al_2O_3	10.18	12.71	12.81	10.98	13.37	11.30	15.61	14.32	14.49	13.96	14.59	12.80	12.69	12.43	13.32	14.19	11.40	12.59	13.11	13.76
Fe_2O_3	10.30	10.92	9.54	12.44	11.48	9.43	7.41	12.97	13.69	10.97	11.28	12.71	10.81	10.98	9.44	5.26	4.69	9.75	13.76	7.70
MgO	2.99	5.23	7.08	7.25	5.51	5.72	2.23	5.07	8.83	7.46	7.43	9.79	5.20	5.10	4.97	2.92	3.50	5.74	8.90	4.15
CaO	20.93	3.34	7.55	8.76	3.52	9.60	3.67	2.75	2.32	2.26	2.00	2.93	2.58	2.09	2.55	2.03	12.15	2.99	4.12	1.90
Na_2O	1.99	2.72	4.86	4.75	2.84	2.06	2.75	2.54	4.26	5.84	6.69	3.93	2.29	2.42	2.90	2.97	2.41	2.21	3.37	2.66
K_2O	0.49	1.63	1.06	0.42	1.71	2.14	1.86	1.16	0.70	0.88	0.65	1.32	2.19	3.02	2.92	4.45	3.59	3.05	1.93	4.88
TiO_2	0.83	0.84	0.80	0.67	0.89	0.86	0.87	1.06	1.11	0.97	1.03	1.05	0.99	0.83	0.86	0.50	0.32	0.97	1.29	0.82
MnO	0.99	0.04	0.13	0.36	0.04	0.18	0.04	0.06	0.15	0.12	0.12	0.19	0.06	0.05	0.05	0.03	0.20	0.13	0.11	0.07
P_2O_5	0.12	0.11	0.09	0.07	0.11	0.15	0.09	0.11	0.10	0.09	0.12	0.12	0.14	0.15	0.14	0.11	0.09	0.18	0.09	0.15
LOI	17.16	10.00	9.27	10.71	4.89	11.60	6.48	6.57	6.67	6.27	6.95	6.03	8.29	5.05	4.34	2.50	10.10	6.72	3.65	4.31
Total	**99.38**	**99.84**	**99.76**	**99.65**	**99.37**	**99.23**	**99.91**	**99.53**	**99.41**	**99.58**	**99.67**	**99.94**	**99.88**	**100.06**	**99.58**	**99.59**	**99.57**	**100.01**	**100.23**	**99.45**
Mg#	39.01	51.35	62.02	56.18	51.35	57.17	39.82	46.25	58.69	59.94	59.19	62.90	51.44	50.55	53.71	55.05	62.19	56.44	58.72	54.28
Trace elements by XRF (ppm)																				
Cr	188.80	201.90	192.50	222.30	103.90	170.10	267.60	160.10	212.00	207.00	203.40	206.90	192.70	194.10	243.80	242.60	138.00	110.60	207.10	188.40
Ni	86.90	56.00	69.20	66.70	43.90	62.90	54.30	65.80	88.70	74.80	78.50	81.40	56.60	48.70	48.70	26.70	28.20	62.10	43.80	64.20
Cu	155.70	102.20	133.50	125.60	54.80	77.00	106.80	163.40	175.40	158.00	170.70	158.70	80.50	55.00	72.10	29.10	22.50	169.20	56.00	80.50
Zn	112.10	109.20	79.30	76.60	71.80	112.10	104.30	130.20	90.80	86.30	90.20	118.40	120.80	117.40	105.40	62.40	46.40	82.90	113.70	127.80
Rb	13.39	40.83	20.52	11.28	61.64	57.02	46.26	38.22	15.90	18.31	15.00	26.56	56.51	94.01	75.31	101.05	78.53	25.35	110.00	74.81
Sr	120.91	326.40	103.58	60.07	164.31	120.91	310.42	194.83	112.25	91.62	80.49	129.05	333.93	246.80	394.35	378.78	261.75	95.85	176.17	130.50
Y	52.10	16.08	19.71	12.65	17.19	29.70	13.35	35.35	23.24	29.30	32.73	27.98	26.67	25.77	25.77	12.55	21.02	40.29	24.05	31.52
Zr	52.56	120.69	56.11	44.35	113.80	154.86	117.24	91.59	89.36	65.84	66.15	123.12	192.37	186.29	215.59	126.06	79.12	91.39	146.95	201.80
Nb	2.21	3.85	2.00	1.49	6.73	9.09	6.01	6.11	2.41	1.90	1.70	4.06	8.88	9.19	8.78	7.14	4.16	2.52	12.27	12.07
Ba	64.20	148.70	126.90	39.00	318.60	187.00	276.30	148.70	111.30	140.40	134.30	179.30	304.80	449.00	505.70	916.70	829.80	90.70	595.50	269.70
V	316.50	281.40	301.80	284.50	164.10	261.20	266.70	310.20	348.80	319.90	349.50	333.60	214.30	179.50	192.20	98.30	79.10	380.50	157.80	172.60
Sc	50.40	48.60	50.80	52.20	27.30	40.30	46.90	48.10	56.50	52.00	55.30	54.90	34.60	30.40	31.90	16.30	15.30	60.30	25.80	34.40
La	15.50	8.40	4.90	7.50	11.50	30.60	14.60	18.70	6.30	5.00	10.40	9.10	20.80	21.30	17.90	19.90	28.50	28.00	25.40	4.90
Ce	42.50	23.30	11.90	15.30	24.00	72.40	33.00	54.80	12.00	12.70	26.70	20.90	51.90	53.50	42.50	34.80	41.90	77.20	49.10	14.60
Nd	21.60	13.50	9.30	10.60	14.90	34.10	17.60	27.30	11.50	10.30	16.20	13.90	25.40	24.30	22.20	17.40	18.10	34.50	26.20	12.00

Extended Data Table 1 | Compositional characteristics of volcanic tuffs from the Rockall Plateau in the northeast Atlantic. Analysis of major and trace element compositions of volcanic tuffs from DSDP Site 555 (for stratigraphic context, see Fig. 2a and Extended Data Fig. 1). Note that Mg# = 100 x molecular MgO/(MgO + FeO), where FeO is assumed to be 0.9FeOT.

Sample ID	Depth (mbsl)	Sample type	$^{143}Nd/^{144}Nd$ norm	2 SE	1 SE	ϵNd	Int. error ϵNd (2s)	Corrected 55 Ma $^{143}Nd/^{144}Nd$	Corrected 55 Ma ϵNd
555-65-1 122 cm	643.22	Tuff	0.511593	0.000010	0.000005	-20.38	0.19	0.511547	-21.28
555-69-5 84 cm	686.77	Tuff	0.511695	0.000008	0.000004	-18.40	0.16	0.511650	-19.27
555-64-3 38 cm	635.88	Tuff	0.511612	0.000009	0.000004	-20.01	0.17	0.511562	-21.00
555-61-2 4.5 cm	605.55	Tuff	0.511657	0.000009	0.000005	-19.13	0.18	0.511610	-20.05
555-65-4 14.5 cm	645.34	Tuff	0.511572	0.000008	0.000004	-20.79	0.15	0.511527	-21.67
555-78-3 81 cm	769.11	Hyaloclastite	0.512939	0.000005	0.000003	5.88	0.10	0.512891	4.94
555-78-3 12.5 cm	768.43	Hyaloclastite	0.513026	0.000006	0.000003	7.57	0.11	0.512978	6.63
Published compositions from Macintyre and Hamilton (1984)[73]									
555-69-2 21 cm	681.70	Lava	0.512990	-		7.02	-		
555-69-4 85 cm	685.30	Lava	0.512920	-		5.66	-		
555-76-1 69 cm	747.20	Lava	0.512987	-		6.96	-		
555-90-1 100 cm	880.50	Lava	0.513026	-		7.72	-		
555-96-3 100 cm	940.60	Lava	0.513022	-		7.65	-		

Extended Data Table 2 | Neodymium isotope characteristics of volcanic rocks from the Rockall Plateau. $^{143}Nd/^{144}Nd$ and associated ϵNd measurements of tuffs, lavas and hyaloclastites from DSDP Leg 81 Site 555. The sample ID number includes the site number (555), core box reference (e.g., 65-1), and the depth from the top of a given core (in cm). The $^{143}Nd/^{144}Nd$ ratios and associated ϵNd values are corrected to an age of 55 Ma. Also provided are published $^{143}Nd/^{144}Nd$ and associated ϵNd measurements from Site 555 lavas[73]. Errors on discrete measurements are 2 and 1 standard error (SE).

| Sample ID | 555-62-1 | 555-62-5 | 555-65-1 | 555-67-5 |
Depth in core	118.5 cm	67 cm	107 cm	2.5 cm
Rb	10.32	32.79	18.47	9.79
Ba	46.30	141.40	154.20	41.22
Nb	1.25	2.37	1.37	0.75
La	9.61	7.19	4.50	4.89
Ce	26.40	17.85	9.43	10.39
Sr	75.66	240.40	68.13	39.49
Nd	12.12	9.29	5.34	5.19
Zr	32.56	48.39	34.78	24.19
Y	37.24	12.18	14.99	9.15

Extended Data Table 3 | Trace element composition of volcanic rocks from the Rockall Plateau. Trace element compositions by ICP-MS of selected PETM-age tuffs from Site 555. The associated recoveries of trace elements from standard reference materials are provided in Supplementary Table 2.

	Olivine				Orthopyroxene				Clinopyroxene				Garnet				Spinel		
	Mean D	1σ	n	refs.	**mean D**	1σ	n	refs.	**mean D**	1σ	n	refs.	**mean D**	1σ	n	refs.	**D**	n	ref.
Ce	**0.0003**	0.0002	3	82,89,90	**0.0057**	0.0032	8	82,89,90	**0.0741**	0.0383	23	82,86–92	**0.0205**	0.0166	11	82,87,88,90,92	**0.01**	1	93
Sm	**0.0009**	0.0005	4	82,89,90	**0.0246**	0.0186	8	82,89,90	**0.2423**	0.155	23	82,86–92	**0.2934**	0.2714	11	82,87,88,90,92	**0.01**	1	93
Yb	**0.0194**	0.0165	4	82,89,90	**0.1201**	0.0673	8	82,89,90	**0.3685**	0.1541	22	82,86–92	**3.7042**	1.4169	11	82,87,88,90,92	**0.01**	1	93

Extended Data Table 4 | Distribution coefficients used in melt modelling. Distribution coefficients (D) used in the construction of Fig. 2e. Note that n = number of individual values of D.

Variable	Description
Sampled Variables:	
$B_{FractCO2}$	CO_2 content (wt%) of basalt, expressed as a fraction
O_{Floss}	Fraction of CO_2 lost from the ocean crust
$C_{FractLIP}$	Fraction of LIP that is fully degassed (of CO_2)
h_{SCLM}	Thickness of the SCLM (km)
w_{SCLM}	Width of the SCLM melting zone (km)
$S_{FractCO2}$	Fraction of CO_2 in the SCLM
Constant and Fixed values:	
ρ_{basalt}	Density of basalt (3000 kg/m^3)
ρ_{SCLM}	Density of the SCLM (3200 kg/m^3)
$r_{basaltprod}$	Volumetric rate of basalt production from ridges (m^3/yr)
$r_{LIPprod}$	Volumetric rate of basalt production from LIPs (m^3/yr)
t_{rift}	Duration of rifting (yrs)
l_{SCLM}	Length of ridge-parallel SCLM melting zone (km)
F_{CSCLM}	Fraction of C released from the SCLM (calculated with 0.04, 0.05 and 0.08)
Outputs:	
W_{COcean}	Total weight of carbon released from the ocean crust (Gt)
W_{CSCLM}	Total weight of carbon in the SCLM (Gt)
W_{TotalC}	Total weight of carbon produced from the SCLM and ocean crust (Gt)

Extended Data Table 5 | Inputs used in degassing models. Description of inputs used in modelling of CO_2 fluxes from mid-ocean ridges, large igneous provinces (LIPs), and melting of the sub-continental lithospheric mantle (SCLM). See the Methods for further details and model description.

Variable	Min	Max	Mean	Var	SD	alpha	beta	Variable name in code
Fraction of CO_2 in ridge/LIP basalts	0.002	0.02	0.005	1.30E-05	0.003602244	0.412	2.060	CO2_conc_beta_samples
CO_2 loss fraction from ocean crust	0.05	0.15	0.1	0.000398429	0.019960674	2.625	2.625	CO2_loss_beta
CO_2 loss fraction from LIP basalts	0.9	1	0.95	0.000399757	0.019993932	2.625	2.625	LIP_loss_beta
Thickness of the SCLM (km)	5	25	20	15.78193019	3.972647756	2.766	0.922	SCLM_thickness
Width of the SCLM melting zone (km)	5	30	25	25.09708683	5.009699275	2.400	0.600	SCLM_width
Fraction CO_2 in the SCLM	0.01	0.1	0.05	0.000323156	0.017976531	2.299	2.874	pc

Extended Data Table 6 | Variables used in carbon flux simulations. Description of variables used in the carbon flux simulations (Fig. 3) given best estimates of the minimum, maximum and mean for each variable, based on data and observations (see Methods). We fixed the standard deviation, SD = 0.2 x range. See the Methods for further details and model description.